nature neuroscience

Article

https://doi.org/10.1038/s41593-025-02111-0

Preconfigured neuronal firing sequences in human brain organoids

Received: 29 December 2023

Accepted: 30 September 2025

Published online: 24 November 2025

Check for updates

Tjitse van der Molen[1,2,3,4], Alex Spaeth[2,5], Mattia Chini[6], Sebastian Hernandez[2,5], Gregory A. Kaurala[1,2], Hunter E. Schweiger[2,7], Cole Duncan[1,2], Sawyer McKenna[1], Jinghui Geng[2,5], Max Lim[3,4], Julian Bartram[8], Tobias Gänswein[8], Aditya Dendukuri[9], Zongren Zhang[10], Jesus Gonzalez-Ferrer[1,2], Kiran Bhaskaran-Nair[11], Aidan L. Morson[12], Cole R. K. Harder[7], Linda R. Petzold[9], Dowlette-Mary Alam El Din[13], Jason Laird[13], Maren Schenke[13], Lena Smirnova[13], Bradley M. Colquitt[2,7,14], Mohammed A. Mostajo-Radji[2], Paul K. Hansma[3,10], Mircea Teodorescu[2,5], Andreas Hierlemann[8], Keith B. Hengen[11], Ileana L. Hanganu-Opatz[6], Kenneth S. Kosik[3,4] & Tal Sharf[1,2,14] ✉

Neuronal firing sequences are thought to be the building blocks of information and broadcasting within the brain. Yet, it remains unclear when these sequences emerge during neurodevelopment. Here we demonstrate that structured firing sequences appear in spontaneous activity of human and murine brain organoids, both unguided and forebrain identity directed, as well as ex vivo neonatal murine cortical slices. We observed temporally rigid and flexible firing patterns in human and murine brain organoids and early postnatal murine somatosensory cortex, but not in dissociated primary cortical cultures. These results suggest that temporal sequences do not arise in an experience-dependent manner, but are rather constrained by a preconfigured architecture established during neurodevelopment. By demonstrating the developmental recapitulation of neural firing patterns, these findings highlight the potential of brain organoids as a model for neuronal circuit assembly.

A growing body of experimental evidence supports the notion that intrinsic activity has a central role in brain function, challenging the traditional Jamesian view that higher-order function is an emergent product of sensory input[1]. The mesoscale wiring of the cortex is dominated by recurrent, lognormally distributed networks[2], where only a small fraction of connections directly relay sensory input[3]. This skewed organization is thought to support the ability of neuronal assemblies to generate temporally structured spiking sequences[4–6]. Sequential activity patterns represent discrete and temporally consolidated packets of neuronal activity, considered the basic building blocks of neural coding and information broadcasting within the brain[7]. In mature brain circuits, spiking sequences predict spatial navigation and memory in the murine hippocampus[8], where 'preplay' encodes new experiences from pre-existing sequence motifs[9,10] that arise before experience-dependent representations form (for example, before exploration beyond the nest)[11]. In the murine visual cortex, evoked responses closely mirror spontaneous sequential patterns[12]. Similar phenomena have also been reported in the human cortex, where the replay of sequences underlies episodic memory formation and retrieval[13]. Moreover, spiking sequences in the human cortex organize into a temporal backbone of rigid and flexible sequence elements that are stable over time and cognitive states[14], support visual categorization tasks and encode non-redundant information beyond latency and rate encoding[15].

However, the emergence of spiking sequences during development is not yet well-understood. During the third postnatal week, the murine hippocampus generates spiking sequences that resemble

A full list of affiliations appears at the end of the paper. ✉e-mail: tsharf@ucsc.edu

https://doi.org/10.1038/s41593-025-02111-0

those that will later be produced during navigation in a linear environment[11]. Notably, these sequences emerge in an experience-independent manner and do not improve upon additional experience in the same postnatal week. Whether similar spiking sequences, potentially representing other forms of experience, exist in other brain areas or at earlier developmental stages remains an open question. The existence of such sequences would provide strong evidence in support of the notion that spiking sequences are not experience-dependent but are instead constrained by an innate architecture that is established during neurodevelopment[16].

Brain organoids, three-dimensional (3D)-stem cell-derived models of the mammalian brain that recapitulate key facets of the anatomical organization and cellular composition found in the developing brain[17–19], represent an ideal system for examining intrinsic (that is, sensory-independent) aspects of neurophysiological development. Neurons within brain organoids form functional synapses[19] and establish spontaneous network activity[20,21]. These self-organized neuronal systems contain cellular diversity and cytoarchitecture necessary to sustain complex network dynamics[22] as evidenced by the expression of layer-specific excitatory pyramidal neurons and inhibitory GABAergic interneurons[23,24]. Brain organoids also generate local field potential oscillations that mirror preterm EEG patterns[25], and have been used to model network dynamics associated with rare genetic disorders[26].

Here we analyzed single-unit activity from the following four models of brain development: (1) human induced pluripotent stem cell (iPSC)-derived brain organoids from two independent laboratories[22,27], (2) mouse embryonic stem cell (ESC)-derived cortical organoids of dorsal forebrain identity, (3) ex vivo neonatal murine somatosensory cortex slices and (4) dissociated two-dimensional (2D) primary cortical cultures[28,29]. Across all models, we observed bursting dynamics on the order of 10^2 ms, consistent with biophysical integration time constants that extend beyond single-neuron refractoriness[30,31]. Within organoids and neonatal slices, a subpopulation of neurons generated nonrandom sequential firing patterns, referred to as backbone sequences[14], which were absent in 2D primary cultures. Backbone sequence-generating neurons occupied the tails of right-skewed lognormal firing rate (FR) and connectivity distributions. At the population level, activity partitioned into low-dimensional subspaces delineated by temporally rigid sequences and higher-dimensional subspaces containing more flexible units. Finally, for a stable and flexible computation, theory suggests that neural systems must exist near a regime called 'criticality', characterized by scale-invariant dynamics across timescales[32]. Using temporal renormalization group theory[33], we found that organoids, slices and 2D cultures operate near criticality, with subsets exhibiting correlations spanning multiple timescales. These results suggest that brain organoids recapitulate preconfigured, experience-independent sequence dynamics while maintaining near-critical states, providing insight into organizational principles that underlie the neural code[34].

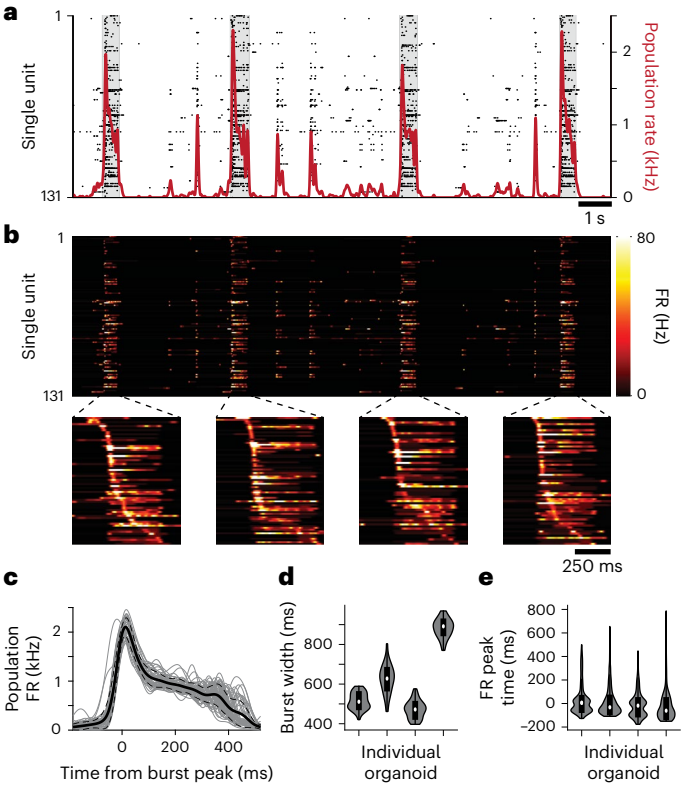

Fig. 1 | Temporal structure of spontaneous single-unit neuronal firing patterns during population bursts in human brain organoids. a, Raster plot of single-unit spiking (black dots) measured across the surface of a 500-µm-thick human brain organoid slice, positioned on top of an MEA. The population FR is shown by the red solid line. Population bursts are marked by sharp increases in the population rate. Burst peak events are denoted by local maxima that exceed 4× r.m.s. fluctuations in the population rate. The shaded gray regions denote the burst duration window as defined by the time interval in which the population rate remains above 10% of its peak value in the burst. **b**, Top: the instantaneous FR of single-unit activity from **a**. Bottom: zoomed-in view of the neuronal firing during population bursts reveals temporal segregation and contiguous tiling of the peak FR of single-unit activity. Here the subsets of units that fire at least twice during the burst are shown, re-ordered for each burst individually based on the time at which the unit has its maximum FR during the burst period. **c**, The population FR (gray lines) is plotted relative to the burst peak for 46 burst events measured across a 3-min interval for the same organoid. The mean value is shown by the solid line and the dashed lines represent 1 s.d. **d**, Burst durations are plotted from four different organoids. **e**, The distribution of single-unit FR peak times relative to population burst peaks for the same organoids as in **d**. Box plots (**d**,**e**)—boxes span the 25th–75th percentiles; the centerline marks the median (50th). Whiskers extend to the most extreme values within 1.5× the interquartile range of the quartile 1 and quartile 3. In violin plots, minima and maxima equal the lowest and highest observations; the shaded area shows the variable's probability density.

Results

Temporal dynamics of neuronal firing sequences in brain organoids

Using high-density complementary metal-oxide-semiconductor (CMOS)-based microelectrode arrays (MEAs)[22], we investigated the temporal dynamics of the spontaneous neuronal activity across guided and unguided human and murine brain organoids. Single-unit spike events revealed population bursts lasting several hundred milliseconds, followed by quiescent periods up to several seconds (Fig. 1a). Moreover, we observed that the distribution of FRs follows a heavy-tailed, right-skewed lognormal distribution ($n = 8$, $R^2 = 0.97 \pm 0.04$; Extended Data Fig. 1a–c). This represents one facet of functional activity conserved across brain regions and states in vivo[3].

Reordering single units by the timing of their peak FR revealed sequential activation patterns during bursts (Fig. 1b). Bursts exhibited consistent rate profiles within organoids (Fig. 1c), with durations spanning timescales on the order of ~10^2 ms (Fig. 1d and Supplementary Fig. 1c). A majority of units' FRs peaked in a close proximity to the population burst maxima (Fig. 1e). These timescales align with spontaneous and evoked sequences in the murine[4] and reptile cortex[5], as well as during memory retrieval in the human cortex[13,14]. Moreover, the dominant neuronal response time of sensory cortices peaks with similar constants across regions and species[30,35,36], suggesting a conserved temporal motif in cortical computation.

To assess stereotypy, we separated units into two classes. Backbone units were defined as those spiking in every burst (Fig. 2a, above dashed line), while all other units were defined as nonrigid (Fig. 2a, below dashed line). Backbone units, residing in the high-firing tail of the lognormal distribution (Extended Data Fig. 1d), displayed stable

https://doi.org/10.1038/s41593-025-02111-0

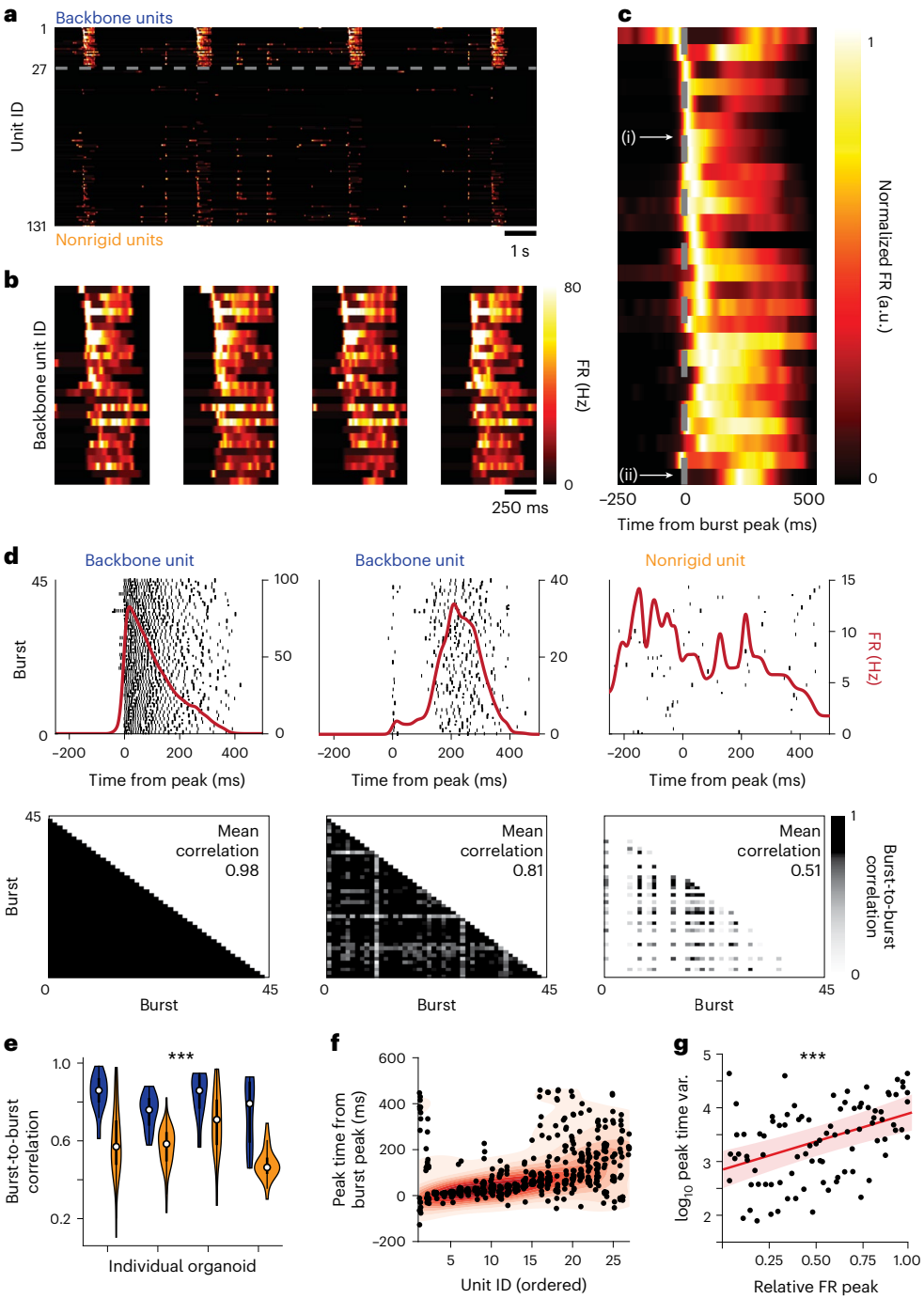

Fig. 2 | Sequential activation patterns in human brain organoids generate a stereotyped temporal backbone. a, Single units were divided into backbone and nonrigid units. Backbone units, defined as spiking at least twice in every burst, are plotted above the dashed line; nonrigid units are below. Within each group, units are ordered by their median firing peak time relative to the burst peak across all bursts and referred to as unit ID. **b**, Zoomed-in view of the backbone units across four bursts with the same unit order. **c**, Average burst peak-centered FRs from 46 burst events. Units maintain the same order in **a** and **b**. Please note the progressive shift in firing peak times relative to the burst peak and an increased spread of activity for units peaking later. **d**, Spiking activity of three units is plotted over a fixed time window relative to burst event peaks. Rows represent spikes from a single burst. Two backbone units are shown with strong temporal alignment to the burst peak and one nonrigid unit with poor alignment. Heatmaps of burst-to-burst cross-correlation coefficients of the burst-centered FRs from the units. **e**, Backbone neurons consistently exhibited higher burst-to-burst correlation coefficients compared to nonrigid units ($P < 10^{-16}$, two-sided linear mixed-effects model, $n = 4$ organoids and 507 single units). Box plots—boxes span the 25th–75th percentiles; the centerline marks the median (50th). Whiskers extend to the most extreme values within 1.5× the interquartile range of the quartile 1 and quartile 3. In violin plots, minima and maxima equal the lowest and highest observations; the shaded area shows the variable's probability density. **f**, FR peak times relative to burst peaks for backbone units. Black dots mark individual bursts, and red shading indicates the probability distribution. **g**, Variance of relative firing peak times for backbone units across four organoids. Units are ordered by median peak time, showing significantly greater variability in later-firing neurons ($P = 1 \times 10^{-6}$, two-sided linear mixed-effects model for relation between relative FR peak and peak time variance). The line represents the mean and the shaded area represents the 95% confidence interval.

temporal delays across bursts (Fig. 2b,c and Extended Data Fig. 2). Clustering bursts by their pairwise correlation matrix confirmed that backbone patterns were preserved across clusters, whereas nonrigid units varied significantly ($P < 10^{-20}$, linear mixed-effects model; Extended Data Fig. 3). Longitudinal recordings showed that the relative fraction of backbone units declined over development (Supplementary Fig. 2). This transition parallels the in vivo incorporation of inhibitory interneurons into maturing excitatory networks[37], also observed histologically in the human (Supplementary Figs. 3 and 4) and murine organoids (Supplementary Figs. 5–7).

To further test the impact of inhibitory tone on backbone neurons, we administered gabazine (10 µM) through bath application to block $GABA_A$ receptors in murine cortical organoids. Gabazine increased burst frequency, backbone participation and their rank-order statistics relative to control conditions. In contrast, blocking AMPA (10-µM NBQX) and NMDA (20-µM R-CPP) receptors, inhibiting excitatory synaptic transmission, abolished bursts, consistent with prior work[22] and eliminated sequences (Extended Data Fig. 4). These findings highlight the dual role of excitation and inhibition in shaping spike timing and sequence rigidity.

To quantify firing consistency during spontaneous bursts, we analyzed single-unit activity relative to the burst peak, following methods used in vivo[4]. Some units displayed sharp peaks with narrow jitter (Fig. 2d, left), others showed delayed but consistent responses (middle), while many lacked preference and fired irregularly (right). Backbone units, comprising 28% ± 14% (mean ± s.d.) of total neurons ($n = 8$ organoids; Supplementary Fig. 1), displayed significantly higher burst-to-burst correlations (Fig. 2e). Their firing patterns remained stable across hours (Supplementary Fig. 8) and persisted over months, with correlations increasing during development in both human and murine organoids (Supplementary Fig. 2c; $P < 10^{-5}$, two-way analysis of variance). Randomized spike trains that preserved mean and single-unit FRs abolished sequences and substantially reduced burst-to-bust correlations (Extended Data Fig. 5 and Supplementary Figs. 9 and 10). This resembled 2D primary cultures with randomized architectures that also lacked sequential firing (Extended Data Fig. 6). Finally, the variability of firing peak times increased with their average latency (Fig. 2f), a relationship consistently observed across organoids (Fig. 2g; $P < 10^{-5}$, linear mixed-effects model). These results indicate that brain organoids can support stereotypical sequential activation with variable dynamics that mirror the propagation of spontaneous activity within the cortical mantle in vivo[4,5,13].

Backbone units are a highly correlated ensemble

To quantify firing patterns during spontaneous bursts, we examined pairwise correlations of single-unit FRs. Backbone units generated stereotyped activation sequences that were preserved across bursts (Fig. 3a). Our analysis of sequential co-activation showed consistent firing onsets and peak times with average phase lags of ~10 ms (Fig. 3b; example units *a* to *b* = 5 ms, example units *b* to *c* = 7 ms), as well as longer lags spanning hundreds of milliseconds between backbone pairs due to the recurring sequential activity (Supplementary Fig. 11). Cross-correlation analysis revealed that backbone units formed a highly correlated ensemble with nonzero phase lags (Fig. 3c,d). Correlation coefficients were significantly higher in backbone compared to nonrigid units (Fig. 3e) and occupied the tail of lognormal distribution (Fig. 3f and Supplementary Fig. 12c–e). Together, these results suggest that a minority population of high-FR neurons is strongly tuned to population dynamics and functions as a stopwatch in the backbone among the more rigid units of the population.

Population FR timing across burst epochs

In previous sections, we analyzed pairwise single-unit relationships. We then asked whether FRs were temporally structured at the population level during bursts. By calculating the cosine similarity of instantaneous FRs across bursts, we observed a sharp similarity peak coinciding with backbone activation, followed by a plateau and decay after burst termination (Fig. 4a,b). Variance in similarity showed the opposite trend—it was high during nonbursting periods, rapidly declining at burst onset and remaining low until bursts ended (Fig. 4c).

Separating units revealed that backbone ensembles displayed substantially higher similarity than nonrigid units or shuffled data (Fig. 4d). Notably, the top 20th percentile of highly correlated units (Fig. 3c) generated substantially higher burst similarity than the full population, with the effect diminishing as larger percentiles were included (Supplementary Fig. 13a,c). Conversely, the lowest 20th percentile reduced similarity, with differences shrinking as more weakly correlated units were added (Supplementary Fig. 13b,c). Across organoids, burst similarity increased at backbone onset and plateaued during their activation (Fig. 4e and Supplementary Fig. 13d; $n = 8$ organoids), underscoring the temporal stability backbone ensembles provide across bursts.

We then examined firing trajectories with principal component analysis (PCA). Burst-related trajectories occupied conserved paths in principal component (PC)-space aligned to burst timing (Fig. 4f, left). When populations were divided, backbone units captured far more variance (73%) in the first two PCs compared to nonrigid units (25%; Fig. 4f, middle and right, Fig. 4g and Supplementary Figs. 14 and 15). Thus, backbone ensembles define a low-dimensional subspace, while nonrigid units exhibit irregular, higher-dimensional dynamics requiring more PCs. Notably, randomization preserving both population and single-unit mean rates abolished these trajectories (Extended Data Fig. 5), demonstrating that structured temporal correlations are not explained by mean FRs alone.

Revealing temporal structure with a hidden Markov model

We previously demonstrated that functional connectivity in human brain organoids follows a heavy-tailed distribution[22], consistent with scaling rules observed in cortical circuits[2]. These motifs are thought to underlie spontaneous activity that propagates broadly across the cortical mantle, mirroring sensory-evoked responses in vivo[4,7]. To further probe this repertoire of dynamics, we applied a hidden Markov model (HMM).

Single-unit activity was binned into 30-ms intervals, capturing fast electrophysiological timescales typical of cortical circuits (~10 to 50 ms)[30], and the HMM was stable over this variable time window (Supplementary Fig. 16). The HMM clustered the data into discrete states, each representing a linear combination of single-unit firing patterns occurring together within bursts. The state transitions are visualized as shaded raster plots aligned closely with burst trajectories (Fig. 5a). Heatmaps of unit firing and histograms of average rates revealed distinct manifolds of activity delineated by differential gain and attenuation across units associated for each state (Fig. 5b). While a 20-state model was used for visualization, similar results were obtained across a range of hidden state counts (Supplementary Fig. 17). Notably, randomized data preserving mean unit and population rates[38] yielded lower log-likelihoods (Supplementary Fig. 18), confirming that the transitions in real data reflected meaningful structure rather than trivial differences explained by the mean rate. The analysis of transitions showed that firing states represent both increases and decreases in relative unit activity (Fig. 5b). Low-probability states appeared before the burst peak, rapidly converged into high-probability transitions at and immediately after the peak, and then relaxed back to low probabilities per unit time (Fig. 5c). This narrowing effect in state space may establish a sequential arrow of time, where initial states preserve more precise timing relative to the following states (Supplementary Fig. 19). As bursts attenuated, the number of states broadened again. The number of realized states during bursts remained similar over a variable range of hidden states, an effect consistent across different hidden state counts (Supplementary Fig. 20), highlighting the robustness of the model.

https://doi.org/10.1038/s41593-025-02111-0

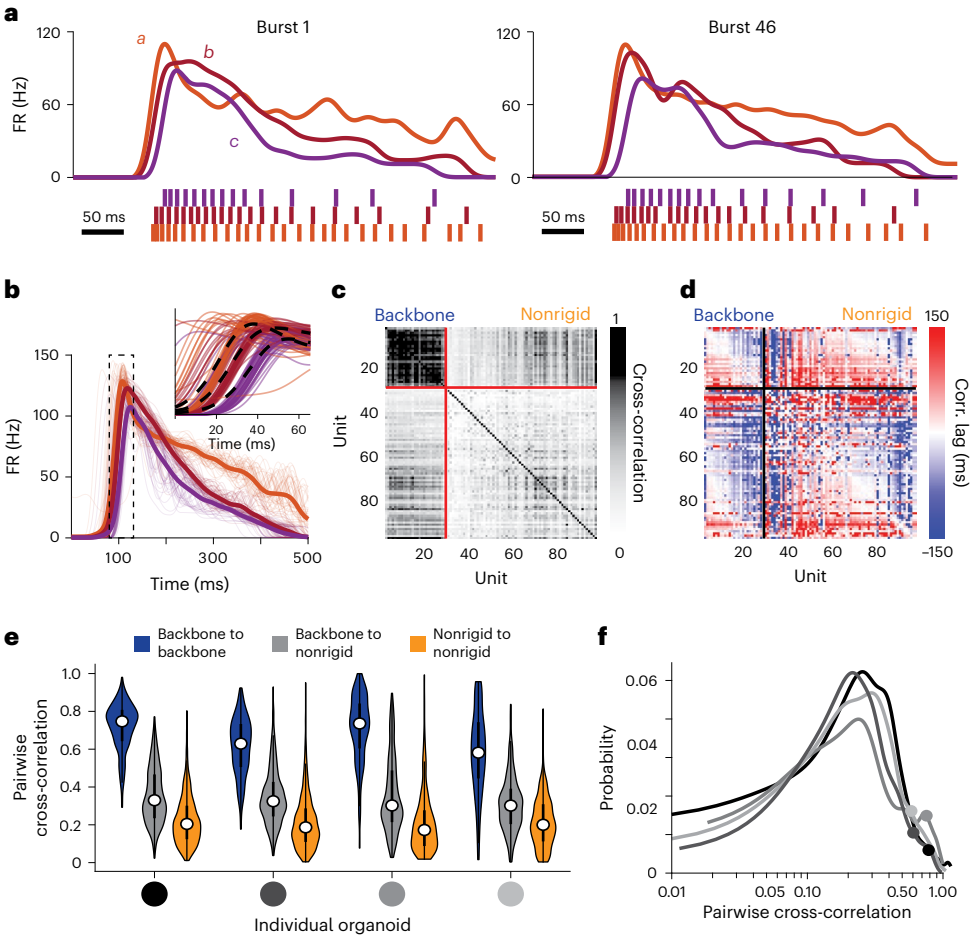

Fig. 3 | Firing patterns between single backbone units within bursts are nonrandom. a, Spike times and computed FRs for three representative units are shown for the first and last burst events of the recording, respectively. **b**, Burst peak-centered average FRs for the three units shown in **a** are calculated over all burst events. The narrow lines indicate the FRs for each individual burst event. The thick lines (dashed black lines in the inset) indicate the average over all bursts. **c**, Pairwise cross-correlation coefficients computed between the instantaneous FRs of all pairs of units with at least 30 spikes counted over all burst events. A maximum lag time of 350 ms was used. The solid red lines separate the backbone units and the nonrigid units. **d**, Lag times leading to the maximum cross-correlation values presented in **c**. Values are clipped at ±150 ms. **e**, Pairwise cross-correlation scores are plotted between unit types. Correlations between backbone units (blue) are significantly higher ($P < 10^{-20}$, two-sided linear mixed-effects model, $n = 4$ organoids and 34,056 single-unit pairs) than the cross-correlations between pairs of backbone and nonrigid units (gray) and pairs of nonrigid units orange). Box plots—boxes span the 25th–75th percentiles; the centerline marks the median (50th). Whiskers extend to the most extreme values within 1.5× the interquartile range from quartile 1 and quartile 3. In violin plots, minima and maxima equal the lowest and highest observations; the shaded area shows the variable's probability density. **f**, The histogram of all pairwise cross-correlations follows a skewed, lognormal distribution (x axis is log scale). The pairwise connections between pairs of backbone units populate the tail of this distribution for all organoids, as can be seen from the distribution means of the backbone-to-backbone distributions in **e** and marked on each histogram (circles on line).

We then asked how these states mapped onto backbone versus nonrigid units. Backbone ensembles spanned a larger pool of HMM states than nonrigid units (Fig. 5d and Supplementary Fig. 21). The PCA of state versus unit realizations revealed separability between these groups by hidden state structure (Fig. 5e). Linear support vector machine classifiers trained on hidden state features distinguished backbone from nonrigid units with 83.9% ± 12.0% accuracy, significantly exceeding the 63.2% ± 10.4% achieved when using FR alone (Fig. 5f). Together, these findings highlight that spontaneous bursts in brain organoids are composed of ensembles, linked together in time to establish neuronal manifolds with temporal structure not observed in randomized data (Supplementary Fig. 22). These manifolds represent a latent multidimensional space of temporally rigid and flexible neuronal subpopulations whose probabilistic trajectories are Markovian in time, namely, future states depend on the system's current state. Such dynamics align with recent experimental and computational models proposing that local pairwise correlations drive irreversibility in noisy logical computations, which contribute to a local arrow of time and generate an irreversible Markovian process independent of sensory input[39].

Endogenous sequences in early developing neonatal cortex

We then asked if spiking sequences also emerge in early developing cortical circuits. Sequential activity patterns are crucial components of mature brain function[7] and support early navigational tasks[11], yet it is not known whether such patterns are present before eye opening and exploration occurs. To address this question, we performed acute extracellular recordings from coronal slices of neonatal murine somatosensory cortex. We observed alternating periods of quiescence and abrupt, synchronized burst events resembling those described in vivo ($n = 6$ slices; Fig. 6a and Extended Data Fig. 7). At this stage, cortical activity is discontinuous, alternating between bursts and quiescent periods, and spike trains are highly correlated[37]. With the exception of olfaction, which controls cognitive maturation[40], most sensory systems remain underdeveloped.

https://doi.org/10.1038/s41593-025-02111-0

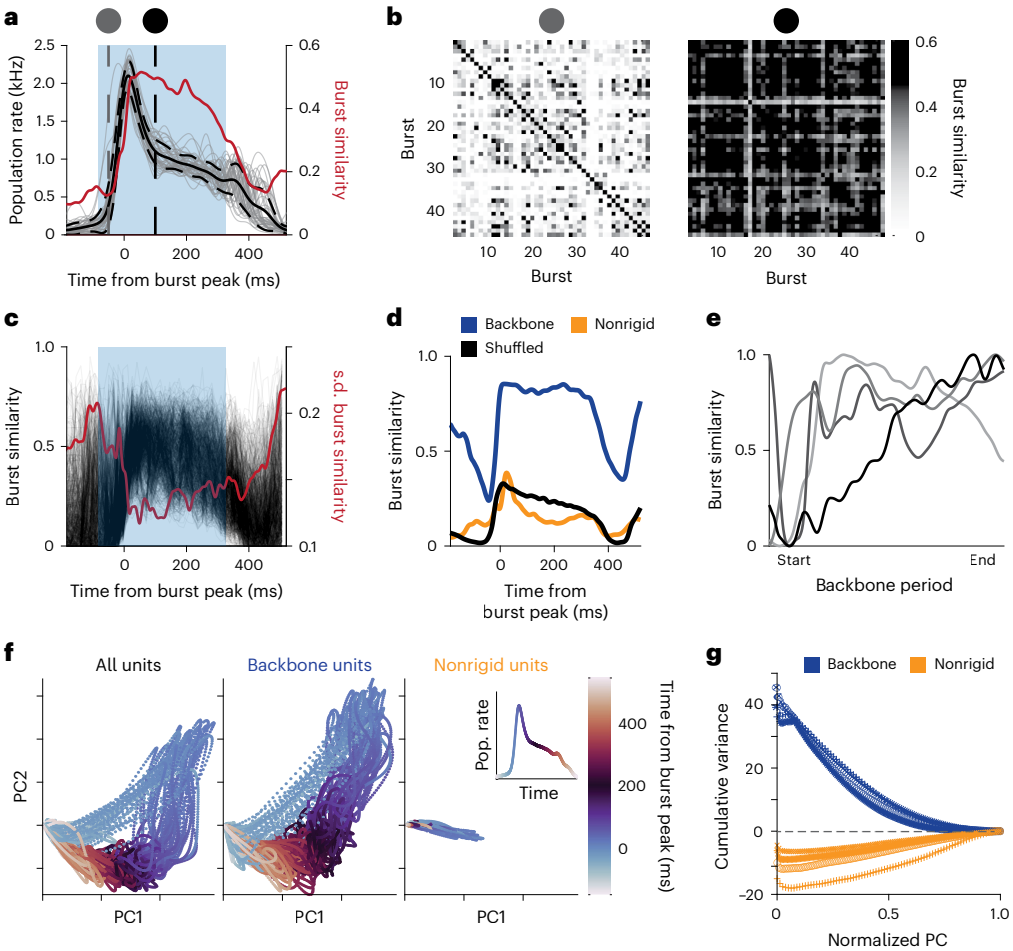

Fig. 4 | Backbone units provide a stable, low-dimensional reference frame for the population bursts. a, Population FRs from 46 burst events from a single human brain organoid are shown relative to burst peaks (gray traces). The mean FR is shown by the solid black line, and the dashed black lines denote the s.d. The red trace shows the average burst similarity score, plotted on the right axis. The blue box highlights the period from the earliest to the latest average FR peak times across all backbone units. **b**, Burst similarity between each pair of bursts is plotted at two reference points—50 ms before the burst peak (left) and 100 ms after the burst peak (right), corresponding to the vertical dashed lines in **a**. **c**, Burst similarity across all pairs of bursts is plotted relative to the burst peak. Each gray line reflects a burst pair, and the red trace represents the s.d. per recording frame. The blue box marks the backbone window described in **a**. **d**, Average similarity computed separately for backbone units, nonrigid units and shuffled data. Backbone units consistently display significantly higher similarity throughout the backbone window compared with nonrigid or shuffled controls ($P < 10^{-20}$, paired two-sided t test). **e**, The average burst similarity increased consistently across organoids following the onset of the backbone period. **f**, Plot of the first two PCs of the single-unit FRs for all units (left), backbone units (middle) and nonrigid units (right). Each dot represents a recording frame and is colored by the time point relative to the closest burst peak. Please note that backbone units reproduce the circular manifold of all units. Nonrigid units lack this trajectory, and variance explained by the first two components is reduced. The inset shows the burst-aligned population rate, color-coded by time relative to the burst peak, illustrating the correspondence between activity and manifold trajectory. **g**, Cumulative variance explained by PCA for backbone (blue) and nonrigid (orange) subsets relative to all units. Across organoids, the first PCs of backbone activity account for more variance than the full population, while nonrigid units account for less.

We then quantified the consistency of firing patterns. Single units were divided into backbone and nonrigid groups based on the recruitment within bursts, after the approach used in organoids (Fig. 6b, Supplementary Fig. 1 and Extended Data Fig. 7). Averaging each unit's firing relative to burst peaks revealed sequential activity among backbone units consistently recruited during bursts (Fig. 6c). Analysis of spike times confirmed preserved temporal offsets between unit peaks with consistent shifts between their peak FRs (Fig. 6d). As in organoids, backbone units formed a strongly correlated core compared to nonrigid units (Fig. 6e–g and Supplementary Figs. 9 and 12), with that activity generating temporal sequences that spanned ~10^2 ms timescales. Together, these results demonstrate that slices of the developing murine somatosensory cortex generate both rigid and flexible firing patterns that establish sequential activation patterns commonly observed in mature cortical circuits across a range of species and brain regions[7].

Comparing sequences across neurodevelopmental models

To understand the role of three dimensionalities in neurodevelopment, we compared neuronal firing patterns generated by 2D murine primary cortical cultures to those observed in human and murine brain organoids and acute murine neonatal slices. All four systems displayed population bursts with consistent firing units recruited during burst epochs (Supplementary Fig. 1). Backbone neurons had significantly higher FRs than nonrigid counterparts (Fig. 7a, $P < 10^{-6}$, linear mixed-effects model, and Supplementary Fig. 23). However, primary cultures exhibited overall higher FRs across both populations ($P < 10^{-10}$ for human organoids and neonatal slices). In contrast, backbone units in organoids and neonatal slices showed significantly stronger normalized burst-to-burst single-unit firing correlations compared to primary cultures (Fig. 7b and Supplementary Fig. 9). After normalization relative to randomized data, backbone units remained significantly more correlated than nonrigid units in organoids and

https://doi.org/10.1038/s41593-025-02111-0

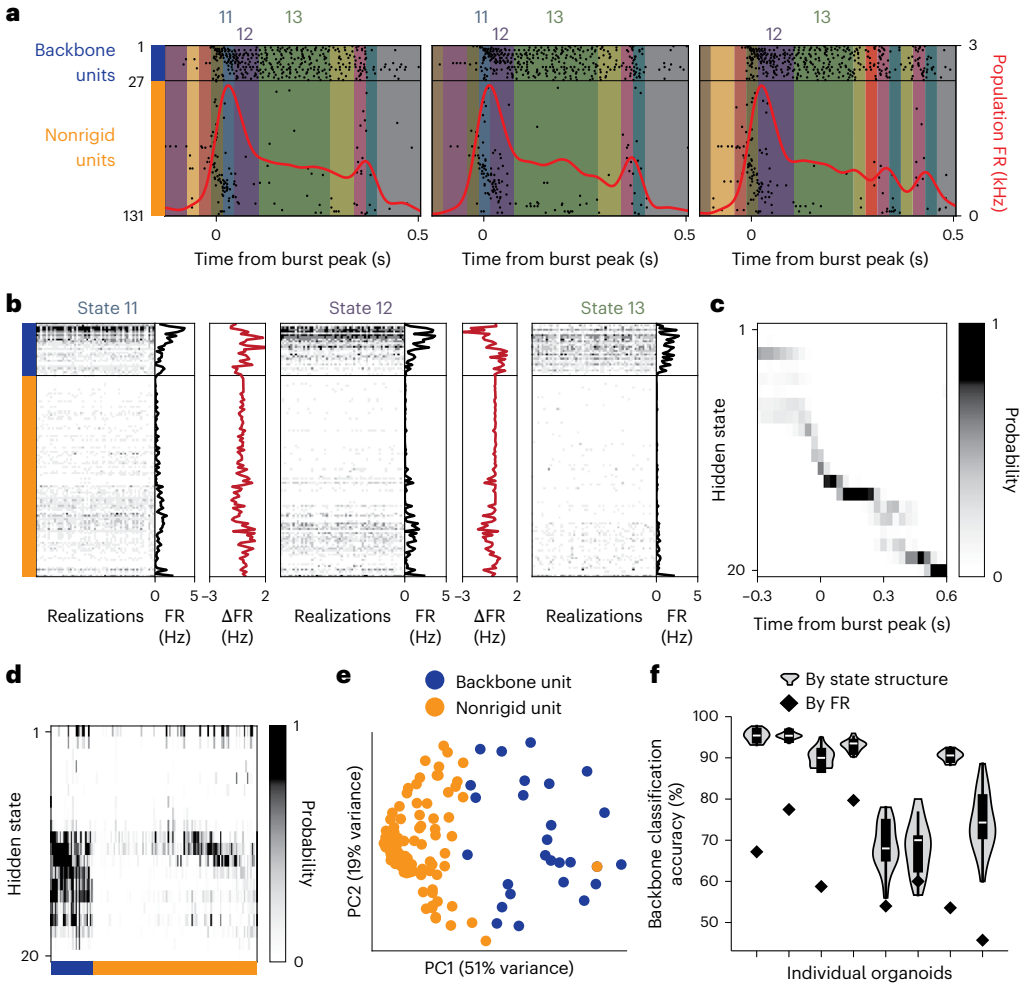

Fig. 5 | HMMs explore stable trajectories and population motifs. a, Repeated sequences of discrete hidden states are shown during three example bursts. The HMM assigns each 30-ms bin of spiking activity a hidden state, represented by background colors. The stereotyped trajectory of these states is visible both in the sequence of state transitions and in the population FR (red trace). Spiking events are shown as a raster, with 27 backbone units displayed above and 104 nonrigid units below a dividing line. **b**, Each hidden state represents a stochastic but repeated activity pattern across units. Example realizations of three states are displayed as heatmaps, along with subpanels showing the average FR of each unit and their difference between adjacent states (ΔFR, red). **c**, The sequence of hidden states follows a stereotyped path across bursts. Heatmap of state probabilities relative to the burst peak shows low variability during the first 0.3 s, corresponding to the structured backbone sequence, with significantly higher variability before the burst begins and later in the burst. **d**, The probability of unit activity across hidden states is displayed as a heatmap. Backbone units (blue) remain consistently active across multiple states, including those outside the burst peak states 11 and 12. Nonrigid units (orange) are active in various states. **e**, Backbone and nonrigid units are nearly linearly separable when classified by their consistency across states. The first two PCs of vectors represent each unit as the sequence of its consistency across states. Backbone and nonrigid units are indicated with color. **f**, FR alone is insufficient to classify units. Violin plots show linear separability scores across fitted HMMs from eight organoids. State-based classification substantially outperforms FR-based classification (diamond marker) in all cases (two-sided Student's *t* test, $P = 0.00021$, $n = 8$ organoids). Box plots (**f**)—boxes span the 25th–75th percentiles; the centerline marks the median (50th). Whiskers extend to the most extreme values within 1.5× the interquartile range of the quartile 1 and quartile 3. In violin plots, minima and maxima equal the lowest and highest observations; the shaded area shows the variable's probability density.

slices ($P < 10^{-10}$ and $P = 7 \times 10^{-4}$, linear mixed-effects model), whereas no significant difference was observed in primary cultures ($P = 0.06$). Despite variability between batches, these differences were consistent across human and murine organoids, across whole and sliced preparations measured in different laboratories (Extended Data Figs. 2 and 8 and Supplementary Fig. 9).

Pairwise cross-correlations further underscored the differences between single-unit FRs among backbone and nonrigid units (Fig. 7c and Supplementary Fig. 12). Backbone-to-backbone pairs in organoids and slices exhibited significantly higher correlations compared to randomized controls ($P < 10^{-10}$, linear mixed-effects model), an effect not observed in primary cultures ($P > 0.99$). These differences were observed in organoids across developmental time points (Supplementary Fig. 2b–d), across different cell lines and human organoid protocols and laboratories[22,27] (Extended Data Fig. 2f), and in murine forebrain organoids (Supplementary Figs. 5 and 12). In contrast, 2D primary cultures exhibited synchronous, burst-centered activity that lacked sequential structure (Extended Data Fig. 6c), identical to randomized organoid data (Extended Data Fig. 5c). Consequently, human and murine organoids showed significantly larger cross-correlation lag times among backbone pairs compared to primary cultures (Fig. 7d; $P < 10^{-7}$ and $P = 0.011$), highlighting their ability to sustain correlated activity on ~10^2 ms timescales typical of cortical and subcortical circuits with the capacity to support sequential firing patterns[7,30,34,36].

We then applied PCA to quantify variance explained by backbone and nonrigid units. In organoids, backbone units explained a significantly larger fraction of variance than other model types (Fig. 7e and Supplementary Fig. 15; $P < 0.001$, linear mixed-effects model). These

https://doi.org/10.1038/s41593-025-02111-0

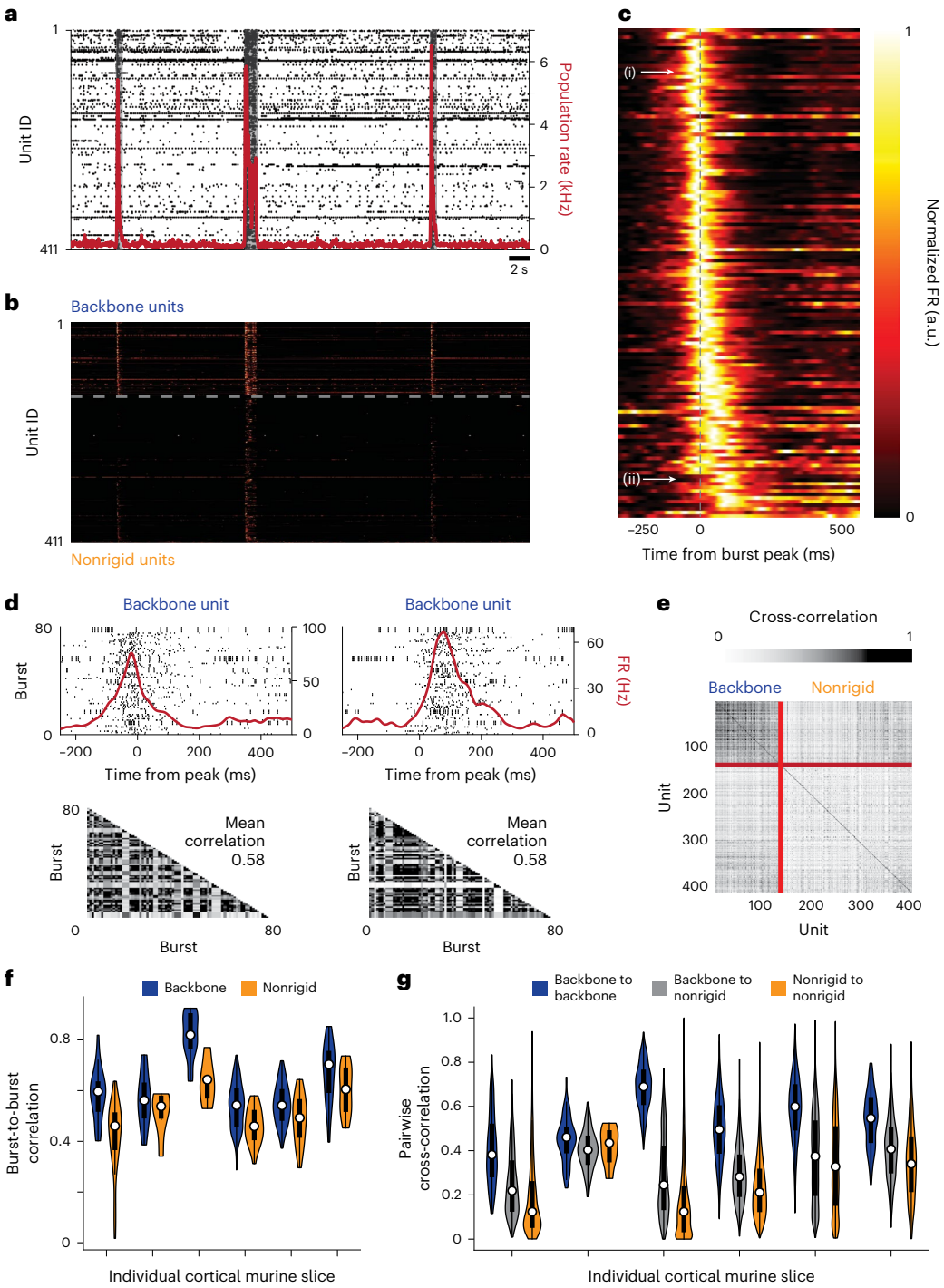

Fig. 6 | Recurring sequential activation patterns in murine neonatal cortical slices generate a stereotyped temporal backbone. a, Raster plot of single-unit spiking recorded from the somatosensory cortex of a P13 murine neonatal brain slice placed on an MEA. The red trace shows the population FR, with bursts marked by sharp increases. Burst peaks are denoted by local maxima that exceed 4× r.m.s. fluctuations in the population rate. Shaded gray regions denote burst durations, defined as intervals where the population rate remains above 10% of its peak. **b**, Instantaneous FRs of units from **a** after reordering. Backbone units are plotted above the dashed line, nonrigid units below. Units are ordered by their median FR peak time relative to the burst peak. For slices, backbone units were defined as spiking at least twice in ≥90% of bursts. **c**, Average burst peak-centered FRs across all bursts. Units maintain the same order as in **b**. A progressive delay in peak times relative to the burst peak is observed, with later-firing units showing broader activity windows. **d**, Example spike trains for two backbone units across bursts, one aligned near the peak and one delayed, along with corresponding average burst-centered FRs (red). Heatmaps of burst-to-burst correlation coefficients are shown below for the same units. **e**, Pairwise cross-correlations of instantaneous FRs from all units with ≥30 spikes. Backbone and nonrigid groups are separated by red lines. **f**, Average burst-to-burst correlations for backbone and nonrigid units for all neonatal cortical slices. Backbone units consistently exhibited higher correlations than nonrigid units ($P < 10^{-20}$, two-sided linear mixed-effects model, $n = 6$ mice and 959 single units). **g**, Pairwise correlations from all unit pairs grouped as backbone–backbone, backbone–nonrigid or nonrigid–nonrigid. Backbone–backbone correlations were significantly stronger than mixed or nonrigid pairs ($P < 10^{-20}$, two-sided linear mixed-effects model, $n = 6$ mice and 125,607 single-unit pairs). Box plots (**f**,**g**)—boxes span the 25th–75th percentiles; the centerline marks the median (50th). Whiskers extend to the most extreme values within 1.5× the interquartile range of the quartile 1 and quartile 3. In violin plots, minima and maxima equal the lowest and highest observations; the shaded area shows the variable's probability density.

https://doi.org/10.1038/s41593-025-02111-0

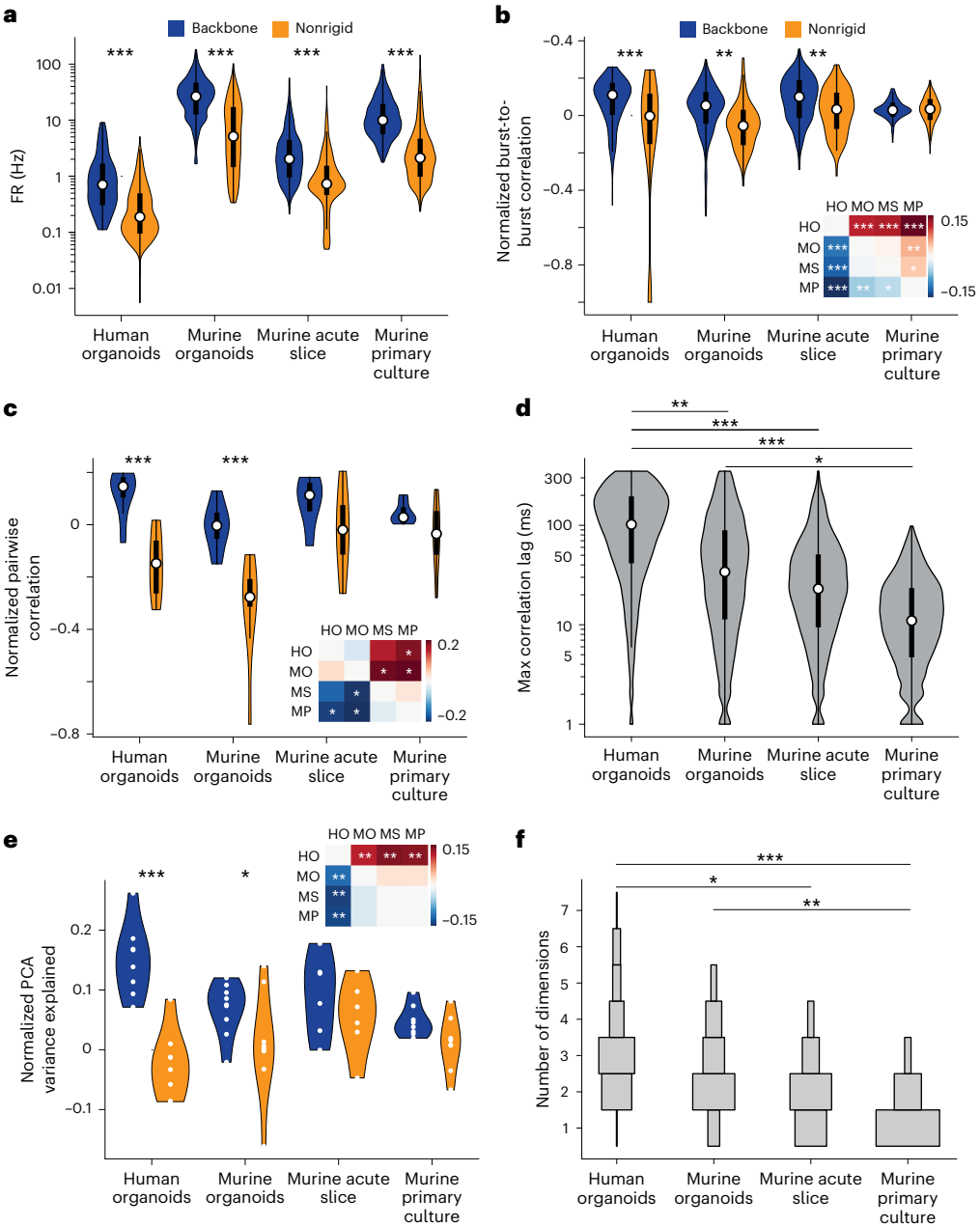

Fig. 7 | Backbone units provide a stable reference frame in brain organoids and murine neonatal cortical slices, but not in murine primary cultures. **a**, Average FR for backbone and nonrigid groups from human brain organoids ($n = 8, 1{,}048$ units), murine cortical organoids ($n = 9, 1{,}179$ units), murine neonatal cortical slices ($n = 6, 786$ units) and murine primary cultures ($n = 8, 1{,}048$ units). Each model type differed significantly from the others, and within each model backbone and nonrigid units were significantly different ($P < 10^{-20}$). **b**, Normalized average burst-to-burst correlations grouped as in **a**. Significant differences were observed between model types and between backbone and nonrigid units for organoids and slices (human organoids, $P < 10^{-20}$; murine organoids, $P = 0.0011$; murine slices, $P = 0.0066$; murine primaries, $P = 0.93$). **c**, Normalized pairwise cross-correlations grouped into backbone–backbone and nonrigid–nonrigid pairs. Backbone pairs showed significantly higher correlations in organoids (human, $P = 9 \times 10^{-7}$; murine, $P = 1 \times 10^{-8}$), but not in slices ($P = 0.10$) or primaries ($P = 0.16$). **d**, Correlation lag times between backbone units were larger for organoids compared to primary cultures (human organoid versus primary, $P = 1 \times 10^{-8}$; murine organoids versus primary, $P = 0.011$), with human organoid differing from murine organoids ($P = 0.0096$) and slices ($P = 0.0002$). Murine organoids versus slices ($P = 0.47$) and primary cultures were not significant ($P = 0.53$). **e**, Normalized variance explained by the first three PCs for all units, backbone and nonrigid groups. Differences were significant for organoids (human, $P = 2 \times 10^{-7}$; murine, $P = 0.036$), but not slices ($P = 0.29$) or primaries ($P = 0.21$). **f**, HMMs revealed higher-dimensional state-spaces in organoids compared with primary cultures. Dimensionality was defined as the number of components explaining 75% of variance. Organoids required more dimensions than primaries (human, $P = 1.2 \times 10^{-6}$; murine, $P = 0.0026$), but not compared with slices (human versus slices, $P = 0.036$; murine versus slices, $P = 0.51$). A two-sided linear mixed-effects model with interactions for unit type and model type was used for **a**–**f** (sample sizes in **a**). Box plots (**a**–**d**)—boxes span the 25th–75th percentiles; the centerline marks the median (50th). Whiskers extend to the most extreme values within 1.5× the interquartile range of the quartile 1 and quartile 3. In violin plots, minima and maxima equal the lowest and highest observations; the shaded area shows the variable's probability density.

findings highlight that organoids generate sequential patterns residing in a lower-dimensional subspace (explained by fewer PCs) embedded within a higher-dimensional background of irregular activity. Neonatal slices also contained backbone units capable of generating sequences that span ~10^2 ms timescales, but with less stereotypy than organoids. By contrast, recurring sequential activation was not sustained in 2D primary cultures.

We then asked if our analysis using HMMs would provide further insight. Across models, nonrigid units were predominantly Poisson, while backbone units were non-Poisson (Supplementary Fig. 24). In the in vivo cortex, Poisson randomness is not universal[31], where architectonically defined regions generate homologous firing patterns that differ systematically across brain regions but remain conserved across species[41]. To compare complexity across models, we defined dimensionality as the number of PCs required to explain a fraction θ of HMM variance. With $\theta = 0.75$, human organoids were separable from slice data ($P = 0.04$, linear mixed-effects model with Poisson observations), while primary cultures had significantly lower dimensionality than both human ($P < 0.0001$) and murine organoids ($P = 0.003$; Fig. 7f), with similar trends existing for a range of values of θ (Supplementary Fig. 25). Within organoids, hidden states captured multidimensional clusters of activity, whereas randomization collapsed them to a one-dimensional space that scales with the population rate (Supplementary Fig. 22). Although the number of realized states was relatively insensitive to the number of hidden states (Supplementary Fig. 20), traversal rates differed—3D models exhibited lower rates than 2D primary cultures (Supplementary Fig. 26).

Firing pattern stability

Despite similarities in firing patterns and stable sequences observed in organoids and neonatal slices, 2D counterparts are dominated by Poisson-like irregularity, which precludes the generation of sustained temporal patterns and confines state transitions, as defined by HMM, to a lower-dimensional space (Fig. 7f). However, all models are capable of generating complex firing patterns with structured population dynamics across multiple timescales. Across phylogeny, brains and other complex systems exhibit signs of criticality[42]. Criticality is a dynamical state of multiscale, marginally stable dynamics that simultaneously optimizes information transmission, storage, dynamic range, susceptibility and robustness. Criticality is widely considered a homeostatic endpoint in the brain[32], that is, in the intact brain, maintained by sleep[43]. While measurements of criticality traditionally require extended sampling of a system's activity, recent progress solves this problem by applying renormalization group theory[33]. We used this framework to quantify how close neural dynamics are to temporal scale-invariance. At criticality, temporal correlations span many timescales without a characteristic scale, captured by the distance metric d_2. Values between 0.0 and 0.1 indicate near-critical dynamics that span many timescales without a characteristic scale, while larger values reflect deviation. A subset of all preparations produced activity consistent with autoregressive models and exhibited near-critical dynamics (Supplementary Fig. 27). Spike-time shuffling consistently abolished temporal criticality across preparations, producing significantly larger d_2 values ($P < 10^{-10}$ compared to intact data, two-sided Welch t test). Murine organoids showed particularly strong agreement between empirical data and model predictions. This indicates that the capacity for scale-invariant dynamics may be a fundamental property of neural circuits that emerges during development, independent of precise circuit architecture or environmental context.

Discussion

Neuronal sequences are believed to form the basis for information broadcasting and computation in the brain[4,6,8–11]. Whether such sequences are emergent features of early brain development, a stage dominated by spontaneous activity with the potential to encode information, remains unclear[34]. We report that temporally structured neuronal sequences emerge in human and murine brain organoids that assemble in the absence of sensory experience. We identify a subpopulation of temporally rigid, sequence-generating 'backbone' neurons that reside in a low-dimensional subspace. In contrast, we found a larger population with more irregular activity, residing in higher-dimensional space. Sequence-generating backbone neurons were also observed in neonatal murine cortical slices that developed under minimal sensory input, but were absent in 2D murine cortical cultures where intrinsic anatomical organization is disrupted. Our results support the hypothesis that neuronal sequences are 'preconfigured' as an innate 3D architecture established during neurodevelopment, arising independent of experience.

To address the open questions above, we leveraged state-of-the-art high-density extracellular recordings from 3D-stem cell-derived models of the human and murine brain, known as brain organoids, which represent an intrinsically self-organized neuronal system that recapitulates key facets of early brain development[17–20] and the establishment of functional circuits[21,22,26]. Our results demonstrate that temporally rigid sequences represent a subpopulation that projects back onto a minority of strong functional connections with a lognormal distribution (Fig. 3). In a seminal paper, it has been demonstrated that emergent computational properties from simple properties of many cells, rather than complex circuits, are capable of generalization and time sequence retention[44]. Therefore, it's not surprising that the temporal structure of spontaneous and evoked patterns of cortical circuits is similar[45,46], because such representations are drawn from a functionally connected neuronal pool with right-skewed, lognormal scaling rules[2].

Units that fire within neuronal sequences exhibit varying temporal precision. Neurons firing at the beginning of population bursts are most constrained, whereas later-firing units are more flexible (Fig. 2f,g). An analogous organization is present in rat somatosensory and auditory cortex[4] and the three-layered turtle cortex[5]. In the hippocampus, experience-dependent replay emerges from spontaneous, experience-independent preconfigured sequences[11]. The balance between temporally correlated and irregular spiking populations is essential for information processing. For example, large-scale recordings from mouse visual cortex and monkey brain reveal a low-dimensional subspace of neurons entrained to population dynamics, insensitive to external stimuli[38]. Similarly, in organoids we observe a backbone subspace embedded within higher-dimensional irregular activity (Fig. 4). Stochastic firing in randomized organoid data closely mirrors 2D dissociated cortical cultures, which show culture-wide synchronization that cannot sustain sequential patterns (Extended Data Figs. 5 and 6), likely reflecting highly redundant 2D network configurations. These findings highlight that neurogenesis and synaptogenesis in organoids generate structured networks rather than random assemblies. Our results support the hypothesis that construction of complex networks capable of recapitulating in vivo neural dynamics requires morphogenesis in three dimensions. Indeed, recent work has demonstrated that human brain organoid circuits, when combined with a machine interface, can act as reservoirs for computing, including speech recognition and nonlinear equation prediction[47].

In vivo, a minority pool of strongly correlated neurons has been proposed to form a fast-acting system embedded within a more weakly coupled background, functioning as a preconfigured brain state[3]. The balance between rigid and flexible spiking and the emergence of sequential patterns are features of 3D cytoarchitecture, supported by our analysis of spontaneous activity in the neonatal murine somatosensory cortex (Fig. 6). A neurophysiological backbone is likely organized during neurogenesis, as pyramidal progenitors establish high-firing subnetworks that remain functionally connected across brain states[16]. In human and murine organoids, highly correlated backbone units increase in burst-to-burst correlation over development (Supplementary Fig. 2). This transition coincides with the incorporation

of inhibitory interneurons[22,48] and reflects an excitatory–inhibitory balance shifting toward inhibition observed in vivo[37], while preserving right-skewed functional rules[49]. Temporal rigidity of sequences is strongly modulated by GABAergic inhibition (Extended Data Fig. 4), where blockade induces heightened burst synchronization, consistent with GABA's inhibitory role. These results underscore interneuron signaling as critical for network homeostasis and for shaping early dynamics before sensory input[37]. Although GABA was once thought to be excitatory during the early development[50], growing evidence indicates inhibitory effects occur much earlier[37,51,52]. Our findings align with this perspective, highlighting interneurons as key contributors to the temporal structure of early neuronal sequences. Brain organoids thus provide a powerful platform to study how specific cell types and regional interactions assemble functional microcircuits[53,54].

Brain organoids represent a self-organized neurodevelopmental system that operates as a closed system devoid of external input, yet capable of generating activity patterns resembling early brain dynamics. Within these firing patterns, we observed overlap between non-Poisson-like activity in organoids and neonatal slices. By contrast, primary cortical cultures with randomized cytoarchitecture showed lower-dimensional state transitions in an HMM (Fig. 7f). In vivo, brain regions balance firing patterns ranging from irregular Poisson to clock-like regularity, depending on local architectures, and these are thought to be critical for higher-order function[31]. In fact, a minority 'backbone' of consistently firing neurons can predict motor control with high accuracy in humans[55] and has been proposed as an 'ansatz', or initial estimate for aligning behavior to environmental input[3]. We posit that highly correlated, non-Poisson components may provide the basis for temporal sequence emergence in development. Early sequences may function as an internal reference for larger-scale dynamics in mature circuits[7], later calibrated by sensory–motor interactions[34]. Indeed, in postnatal murine brain, preconfigured motifs arise spontaneously in rest and are not improved by sequential experience during the third week[11]. We further show that firing in organoids and neonatal slices generates strong nonrandom correlations with temporal jitter and nonzero phase lags. These ensembles form manifolds of trajectories identifiable by an HMM, with a core of strongly interacting units (Fig. 5c,d). Such subsets may act as 'irreversible' noisy logic elements that establish a local arrow of time, similar to recent findings in retinal circuits, neuronal activity remains irreversible even when their inputs are not[39].

In summary, our analysis of spontaneous activity, generated by stem cell-derived human and murine brain organoids, demonstrates that structured spiking sequences can emerge without sensory experience and motor output, supporting the preconfigured brain hypothesis. These results are in line with recent work showing how pharmacologically abolishing all central nervous system activity during the development of the larval zebrafish did not alter an oculomotor behavior[56], suggesting that complex sensory–motor systems are hard-wired by activity-independent mechanisms. Our findings recall the philosophy discussed in ref. 57, which posited an a priori construction of a space-time map that, in modern terms, could serve as a 'scaffold' to enable the brain to interact with and make sense of the world. In conclusion, brain organoids provide a heuristic platform for exploring how exogenous inputs refine self-organized neuronal circuits imbued with the innate capacity to process information and compute[47], while also facilitating new studies into the genetic mechanisms governing the assembly of functional circuitry during early human brain development[58–62].

Online content

Any methods, additional references, Nature Portfolio reporting summaries, source data, extended data, supplementary information, acknowledgements, peer review information; details of author contributions and competing interests; and statements of data and code availability are available at https://doi.org/10.1038/s41593-025-02111-0.

References

1. Llinás, R. R. & Paré, D. Of dreaming and wakefulness. *Neuroscience* **44**, 521–535 (1991).
2. Song, S., Sjöström, P. J., Reigl, M., Nelson, S. & Chklovskii, D. B. Highly nonrandom features of synaptic connectivity in local cortical circuits. *PLoS Biol.* **3**, e68 (2005).
3. Buzsáki, G. & Mizuseki, K. The log-dynamic brain: how skewed distributions affect network operations. *Nat. Rev. Neurosci.* **15**, 264–278 (2014).
4. Luczak, A., Barthó, P. & Harris, K. D. Spontaneous events outline the realm of possible sensory responses in neocortical populations. *Neuron* **62**, 413–425 (2009).
5. Hemberger, M., Shein-Idelson, M., Pammer, L. & Laurent, G. Reliable sequential activation of neural assemblies by single pyramidal cells in a three-layered cortex. *Neuron* **104**, 353–369 (2019).
6. Riquelme, J. L., Hemberger, M., Laurent, G. & Gjorgjieva, J. Single spikes drive sequential propagation and routing of activity in a cortical network. *eLife* **12**, e79928 (2023).
7. Luczak, A., McNaughton, B. L. & Harris, K. D. Packet-based communication in the cortex. *Nat. Rev. Neurosci.* **16**, 745–755 (2015).
8. Pastalkova, E., Itskov, V., Amarasingham, A. & Buzsáki, G. Internally generated cell assembly sequences in the rat hippocampus. *Science* **321**, 1322–1327 (2008).
9. Dragoi, G. & Tonegawa, S. Preplay of future place cell sequences by hippocampal cellular assemblies. *Nature* **469**, 397–401 (2011).
10. Grosmark, A. D. & Buzsáki, G. Diversity in neural firing dynamics supports both rigid and learned hippocampal sequences. *Science* **351**, 1440–1443 (2016).
11. Farooq, U. & Dragoi, G. Emergence of preconfigured and plastic time-compressed sequences in early postnatal development. *Science* **363**, 168–173 (2019).
12. Carrillo-Reid, L., Miller, J.-E. K., Hamm, J. P., Jackson, J. & Yuste, R. Endogenous sequential cortical activity evoked by visual stimuli. *J. Neurosci.* **35**, 8813–8828 (2015).
13. Vaz, A. P., Wittig, J. H., Inati, S. K. & Zaghloul, K. A. Replay of cortical spiking sequences during human memory retrieval. *Science* **367**, 1131–1134 (2020).
14. Vaz, A. P., Wittig, J. H., Inati, S. K. & Zaghloul, K. A. Backbone spiking sequence as a basis for preplay, replay, and default states in human cortex. *Nat. Commun.* **14**, 4723 (2023).
15. Xie, W. et al. Neuronal sequences in population bursts encode information in human cortex. *Nature* **635**, 935–942 (2024).
16. Huszár, R., Zhang, Y., Blockus, H. & Buzsáki, G. Preconfigured dynamics in the hippocampus are guided by embryonic birthdate and rate of neurogenesis. *Nat. Neurosci.* **25**, 1201–1212 (2022).
17. Eiraku, M. et al. Self-organized formation of polarized cortical tissues from ESCs and its active manipulation by extrinsic signals. *Cell Stem Cell* **3**, 519–532 (2008).
18. Lancaster, M. A. et al. Cerebral organoids model human brain development and microcephaly. *Nature* **501**, 373–379 (2013).
19. Birey, F. et al. Assembly of functionally integrated human forebrain spheroids. *Nature* **545**, 54–59 (2017).
20. Quadrato, G. et al. Cell diversity and network dynamics in photosensitive human brain organoids. *Nature* **545**, 48–53 (2017).
21. Giandomenico, S. L. et al. Cerebral organoids at the air–liquid interface generate diverse nerve tracts with functional output. *Nat. Neurosci.* **22**, 669–679 (2019).
22. Sharf, T. et al. Functional neuronal circuitry and oscillatory dynamics in human brain organoids. *Nat. Commun.* **13**, 4403 (2022).
23. Qian, X. et al. Sliced human cortical organoids for modeling distinct cortical layer formation. *Cell Stem Cell* **26**, 766–781 (2020).
24. Wang, Y. et al. Modeling human telencephalic development and autism-associated SHANK3 deficiency using organoids generated from single neural rosettes. *Nat. Commun.* **13**, 5688 (2022).

25. Trujillo, C. A. et al. Complex oscillatory waves emerging from cortical organoids model early human brain network development. *Cell Stem Cell* **25**, 558–569 (2019).
26. Samarasinghe, R. A. et al. Identification of neural oscillations and epileptiform changes in human brain organoids. *Nat. Neurosci.* **24**, 1488–1500 (2021).
27. Alam El Din, D.-M., et al. Human neural organoid microphysiological systems show the building blocks necessary for basic learning and memory. *Commun. Biol.* **8**, 1237 (2025).
28. Yuan, X. et al. Versatile live-cell activity analysis platform for characterization of neuronal dynamics at single-cell and network level. *Nat. Commun.* **11**, 4854 (2020).
29. Bartram, J. et al. Parallel reconstruction of the excitatory and inhibitory inputs received by single neurons reveals the synaptic basis of recurrent spiking.*eLife* **12**, RP86820 (2024).
30. Koch, C., Rapp, M. & Segev, I. A brief history of time (constants). *Cereb. Cortex* **6**, 93–101 (1996).
31. Maimon, G. & Assad, J. A. Beyond Poisson: increased spike-time regularity across primate parietal cortex. *Neuron* **62**, 426–440 (2009).
32. Ma, Z., Turrigiano, G. G., Wessel, R. & Hengen, K. B. Cortical circuit dynamics are homeostatically tuned to criticality in vivo. *Neuron* **104**, 655–664 (2019).
33. Wilson, K. G. The renormalization group: critical phenomena and the Kondo problem. *Rev. Mod. Phys.* **47**, 773–840 (1975).
34. Dragoi, G. The generative grammar of the brain: a critique of internally generated representations. *Nat. Rev. Neurosci.* **25**, 60–75 (2024).
35. Derdikman, D., Hildesheim, R., Ahissar, E., Arieli, A. & Grinvald, A. Imaging spatiotemporal dynamics of surround inhibition in the barrels somatosensory cortex. *J. Neurosci.* **23**, 3100–3105 (2003).
36. Murray, J. D. et al. A hierarchy of intrinsic timescales across primate cortex. *Nat. Neurosci.* **17**, 1661–1663 (2014).
37. Chini, M., Pfeffer, T. & Hanganu-Opatz, I. An increase of inhibition drives the developmental decorrelation of neural activity. *eLife* **11**, e78811 (2022).
38. Okun, M. et al. Diverse coupling of neurons to populations in sensory cortex. *Nature* **521**, 511–515 (2015).
39. Lynn, C. W., Holmes, C. M., Bialek, W. & Schwab, D. J. Decomposing the local arrow of time in interacting systems. *Phys. Rev. Lett.* **129**, 118101 (2022).
40. Chen, Y.-N., Kostka, J. K., Bitzenhofer, S. H. & Hanganu-Opatz, I. L. Olfactory bulb activity shapes the development of entorhinal-hippocampal coupling and associated cognitive abilities. *Curr. Biol.* **33**, 4353–4366 (2023).
41. Mochizuki, Y. et al. Similarity in neuronal firing regimes across mammalian species. *J. Neurosci.* **36**, 5736–5747 (2016).
42. O'Byrne, J. & Jerbi, K. How critical is brain criticality?. *Trends Neurosci.* **45**, 820–837 (2022).
43. Xu, Y., Schneider, A., Wessel, R. & Hengen, K. B. Sleep restores an optimal computational regime in cortical networks. *Nat. Neurosci.* **27**, 328–338 (2024).
44. Hopfield, J. J. Neural networks and physical systems with emergent collective computational abilities. *Proc. Natl Acad. Sci. USA* **79**, 2554–2558 (1982).
45. Kenet, T., Bibitchkov, D., Tsodyks, M., Grinvald, A. & Arieli, A. Spontaneously emerging cortical representations of visual attributes. *Nature* **425**, 954–956 (2003).
46. Han, F., Caporale, N. & Dan, Y. Reverberation of recent visual experience in spontaneous cortical waves. *Neuron* **60**, 321–327 (2008).
47. Cai, H. et al. Brain organoid reservoir computing for artificial intelligence. *Nat. Electron.* **6**, 1032–1039 (2023).
48. Kanton, S. et al. Organoid single-cell genomic atlas uncovers human-specific features of brain development. *Nature* **574**, 418–422 (2019).
49. Chini, M., Hnida, M., Kostka, J. K., Chen, Y.-N. & Hanganu-Opatz, I. L. Preconfigured architecture of the developing mouse brain. *Cell Rep.* **43**, 114267 (2024).
50. Kalemaki, K. et al. The developmental changes in intrinsic and synaptic properties of prefrontal neurons enhance local network activity from the second to the third postnatal weeks in mice. *Cereb. Cortex* **32**, 3633–3650 (2022).
51. Che, A. et al. Layer I interneurons sharpen sensory maps during neonatal development. *Neuron* **99**, 98–116 (2018).
52. Kirmse, K. et al. GABA depolarizes immature neurons and inhibits network activity in the neonatal neocortex in vivo. *Nat. Commun.* **6**, 7750 (2015).
53. Roth, J. G. et al. Spatially controlled construction of assembloids using bioprinting. *Nat. Commun.* **14**, 4346 (2023).
54. Osaki, T. et al. Complex activity and short-term plasticity of human cerebral organoids reciprocally connected with axons. *Nat. Commun.* **15**, 2945 (2024).
55. Carmena, J. M. et al. Learning to control a brain–machine interface for reaching and grasping by primates. *PLoS Biol.* **1**, e42 (2003).
56. Barabási, D. L., Schuhknecht, G. F. P. & Engert, F. Functional neuronal circuits emerge in the absence of developmental activity. *Nat. Commun.* **15**, 364 (2024).
57. Kant, I. *Critique of Pure Reason* (Cambridge University Press, 1998).
58. Birtele, M. et al. Non-synaptic function of the autism spectrum disorder-associated gene SYNGAP1 in cortical neurogenesis. *Nat. Neurosci.* **26**, 2090–2103 (2023).
59. Birtele, M., Lancaster, M. & Quadrato, G. Modelling human brain development and disease with organoids. *Nat. Rev. Mol. Cell Biol.* **26**, 389–412 (2025).
60. Pollen, A. A. et al. Establishing cerebral organoids as models of human-specific brain evolution. *Cell* **176**, 743–756 (2019).
61. Fiddes, I. T. et al. Human-specific NOTCH2NL genes affect notch signaling and cortical neurogenesis. *Cell* **173**, 1356–1369 (2018).
62. Benito-Kwiecinski, S. et al. An early cell shape transition drives evolutionary expansion of the human forebrain. *Cell* **184**, 2084–2102 (2021).

[1]Department of Biomolecular Engineering, University of California, Santa Cruz, Santa Cruz, CA, USA. [2]UC Santa Cruz Genomics Institute, University of California, Santa Cruz, Santa Cruz, CA, USA. [3]Neuroscience Research Institute, University of California, Santa Barbara, Santa Barbara, CA, USA. [4]Department of Molecular, Cellular and Developmental Biology, University of California, Santa Barbara, Santa Barbara, CA, USA. [5]Department of Electrical and Computer Engineering, University of California, Santa Cruz, Santa Cruz, CA, USA. [6]Institute of Developmental Neuroscience, Center for Molecular Neurobiology, Hamburg Center of Neuroscience, University Medical Center Hamburg–Eppendorf, Hamburg, Germany. [7]Department of Molecular,

Cell and Developmental Biology, University of California, Santa Cruz, Santa Cruz, CA, USA. [8]Department of Biosystems Science and Engineering, ETH Zürich, Basel, Switzerland. [9]Department of Computer Science, University of California, Santa Barbara, Santa Barbara, CA, USA. [10]Department of Physics, University of California, Santa Barbara, Santa Barbara, CA, USA. [11]Department of Biology, Washington University in St. Louis, St. Louis, MO, USA. [12]Department of Physics, University of California, Santa Cruz, Santa Cruz, CA, USA. [13]Center for Alternatives to Animal Testing (CAAT), Department of Environmental Health and Engineering, Bloomberg School of Public Health, Johns Hopkins University, Baltimore, MD, USA. [14]Institute for the Biology of Stem Cells, University of California, Santa Cruz, Santa Cruz, CA, USA. ✉e-mail: tsharf@ucsc.edu

Methods

Human brain organoid slice recordings and preprocessing

The human brain organoids extracellular field recordings presented in Figs. 1–4 were sourced from ref. 22. Organoids with less than 20 active units were not considered significant to reliably separate a backbone and nonrigid population. Briefly, brain organoids were grown based on the methods developed in ref. 18 and were of predominant forebrain identity based on the single-cell RNA sequencing analysis[22]. The recordings were made using CMOS MEA technology (MaxOne, MaxWell Biosystems) using MaxLab Live (version 19.2.19). The electrode selection was done based on the automatic activity scans (tiled blocks of 1,020 electrodes) to identify the spatial distribution of electrical activity across the surface of the organoid. The 1,020 most active electrodes were chosen with a minimal spacing distance of at least two electrodes (2 × 17.5 µm), providing sufficient electrode redundancy per neuron to enable accurate identification of single units by spike sorting[63], while simultaneously sampling network activity across the whole organoid surface interfacing the MEA. Measurements were made in a culture incubator (5% CO_2 at 37 °C) with a sampling rate of 20 kHz for all recordings, and the data were saved in HDF5 file format. The raw extracellular recordings were band-pass filtered between 300 and 6,000 Hz and subsequently spike sorted using the Kilosort2 algorithm[64] through a custom Python pipeline. The spike sorting output was then further curated by removing units with an ISI violation threshold[65] above 0.3, an average FR below 0.05 Hz and/or a signal-to-noise ratio below 5.

Whole human brain organoid recordings

Additional electrophysiology data from whole human brain organoids (Fig. 7) were sourced from ref. 27 that made use of high-density MEAs integrated into a six-well configuration (MaxTwo, MaxWell Biosystems). Whole organoids were attached to MEAs at 9.5 weeks old and grown for 32 days. Recordings were performed using the same methods in the previous section using MaxLab Live (version 22.2.6). The organoids were grown from human iPSCs (NIBSC8 iPSC line) and cultured in mTESR Plus medium on vitronectin and differentiated into organoids based on a previously established protocol[66]. Neural differentiation was induced with Neural Induction medium through SMAD inhibition (Gibco) and organoids were differentiated under gyratory shaking (88 rpm, 50-mm orbit) for up to 8 weeks in Neurobasal Plus medium supplemented with 1× B27-Plus, 10 ng ml^{-1} human recombinant GDNF (GeminiBio), 10 ng ml^{-1} human recombinant BDNF (GeminiBio), 1% penicillin–streptomycin–glutamine (Gibco, Thermo Fisher Scientific). Half changes of medium were performed thrice a week. See Supplementary Methods for additional details regarding ESC maintenance, organoid generation, single-cell RNA sequencing and immunohistochemistry characterization.

Murine ESC-derived cortical organoids

Organoids were generated from the following three distinct mouse ESC lines: C57BL/6, E14TG2a (129/Ola) and KH2 (129/SvJ x C57BL/6 hybrid). ESCs were dissociated into single cells using TrypLE Express Enzyme (Thermo Fisher Scientific, 12604021) for 5 min at 37 °C. After dissociation, the cells were re-aggregated in lipidure-coated 96-well V-bottom plates at a density of 3,000 cells per well in 150 µl of mESC maintenance medium, supplemented with 10 µM Rho Kinase Inhibitor (Y-27632; Tocris, 1254) and 1,000 units ml^{-1} Recombinant Mouse Leukemia Inhibitory Factor (MilliporeSigma, ESG1107). After 24 h of re-aggregation, the medium was replaced with cortical differentiation medium (Supplementary Methods).

Daily medium changes were performed, with N-2 and B-27 supplements added postfiltration to preserve their hydrophobic components. On day 5, organoids were transferred to ultralow adhesion plates (MilliporeSigma, CLS3471), where the medium was replaced with fresh neuronal differentiation medium. The plates were then placed on an orbital shaker set to 68 rpm to prevent organoid fusion. To ensure optimal growth conditions, 16 organoids per well were consistently maintained. Organoids were plated whole at an age of around 30 days and recordings started when consistent population bursts were observed, in a similar manner as the human brain organoid slices as described previously. Recordings were performed using MaxLab Live (version 25.1.6; MaxWell Biosystems).

Neonatal murine brain-slice preparation

All experiments involving murine neonatal acute slice recordings were approved by the Basel-Stadt veterinary office according to Swiss federal laws on animal welfare. Animal housing was equipped with an artificial light source providing a daylight-like spectrum. The light phase of the dark/light cycle lasted from 6:30 a.m. to 6:30 p.m., with a 30-min twilight period during both dark-to-light and light-to-dark transitions. Ambient temperature was maintained at 20–24 °C, and relative humidity at 45–65%. Briefly, mouse pups (P12–P14; both sexes; C57BL/6JRj from Janvier Labs) were decapitated under isoflurane anesthesia, followed by brain dissection in ice-cold artificial CSF (aCSF) bubbled with carbogen gas (95% O_2, 5% CO_2). To promote self-sustained cortical activity[67], the following aCSF recipe was used: 126 mM NaCl, 3.5 mM KCl, 1.25 mM NaH_2PO_4, 1 mM $MgSO_4$, 2 mM $CaCl_2$, 26 mM $NaHCO_3$ and 10 mM glucose, at approximately pH 7.3 when bubbled with carbogen. Coronal brain slices (370 µm) were prepared using a vibratome (VT1200S, Leica). Slices were subsequently transferred to a chamber submerged in carbogenated aCSF and stored at room temperature until use.

Acute recordings from neonatal murine brain slices

For recordings, a brain slice containing somatosensory cortex was transferred from the storage chamber onto the sensing area of the CMOS MEA and fixated with a customized MaxOne Tissue Holder (MaxWell Biosystems). The slice was perfused with heated aCSF (32–34 °C). Recordings were performed using MaxLab Live (version 22.2.8; MaxWell Biosystems). Sparse, rectangular electrode configurations were selected to find active regions of the somatosensory cortex, with a sparsity of two or three to allow for a good spike-sorting performance.

Primary planar culture preparation

The presented primary neuronal recordings (Pr) were sourced from ref. 28 for Pr1–Pr4 and from ref. 29 for Pr5–Pr8. Briefly, neuronal cultures were prepared from embryonic day 18 Wistar rat cortices and plated at a density of 3,000 cells per mm^2 onto high-density CMOS MEAs (MaxOne, MaxWell Biosystems) and maintained in a cell culture incubator (5% CO_2 at 37 °C)[28]. The recordings were made at 20 days in vitro. The recordings can be obtained from https://www.research-collection.ethz.ch/handle/20.500.11850/431730.

Comparing data from different sources

No statistical methods were used to predetermine sample sizes, but our sample sizes are similar to those reported in previous publications[22,27–29,67]. The recording durations of all recordings coming from the same source were kept consistent. The recording durations per data source were selected so that each recording contained around 40 bursts (38 ± 4 bursts, mean ± s.e.), using the first x minutes of the recording to get to this value.

Data distributions were assumed to be normal, but this was not formally tested. Where distributions visually deviated from a normal distribution, a log transformation was performed or the distribution was modeled with a generalized linear model. Where data distributions contained a number of samples that were too large to be plotted individually, violin plots were used to report the shape of the distribution. Data analyses were performed blindly to the conditions of the experiments.

Single-unit FR and CV2 calculations scores

All of the following analyses were performed using custom MATLAB scripts. MATLAB (version R2018b) was used. The FR of each individual

spike-sorted unit with at least 30 detected spikes in the recording was computed by obtaining the interspike interval between each spike event and applying a Gaussian smoothing with a 50-ms kernel to its inverse. A lognormal distribution was fitted to the distribution of FRs averaged over the whole recording period for each unit. The goodness of the fit was assessed using the R^2 metric. In addition, for the same selection of units, the CV2 score of the spiking activity was computed per unit as described in ref. 68 as a measure of spiking variability. The same CV2 computations were performed on 100 different shuffled spike matrices and the results from the original spike matrices were *z*-score normalized using the mean and s.d. over all shuffled datasets.

Population rate calculations

The population FR was computed by summing spikes over all units of each frame, followed by smoothing with a 20-ms sliding square window and a subsequent 100-ms sliding Gaussian kernel. For the detection of the burst start, end and peak, population activity bursts were defined when the population-averaged spike rate exceeded 4× its root mean square (r.m.s.) value (using the built-in MATLAB function findpeaks with min_dist = 700 ms. For recordings with long-duration bursts, min_dist was increased up to 2,000 ms to prevent peaks in the tail of the burst from being detected as separate burst instances). The burst start and end times were determined as the first time points where the multi-unit activity fell below 10% of the detected peak value, occurring before and after the burst peaks, respectively. The actual burst peak time was then obtained by recomputing the population FR using a 5-ms square window and a 5-ms Gaussian kernel and finding the frame with the highest value between the burst start and end time. For murine primary planar cultures, a 20-ms square window, a 50-ms Gaussian kernel and a 3× r.m.s. threshold were used for population peak detection and a 20% threshold for the burst start and end time detection. These values were chosen to account for stronger jitteriness of the population activity and more abundant interburst activity.

FR sequences and burst backbones

For each individual unit, the FR centered by the burst peak was averaged from −250 ms to 500 ms relative to the burst peak. In addition, the time relative to the population burst peak, when this unit experienced a peak in its FR within the burst start and end window, was selected. The median and variance of the FR peak times were computed per unit over all bursts in which this unit fired at least two action potentials. The median values were used for reordering the units for different plotting purposes and the variance was used to fit a linear mixed-effects model to study the relationship between the effect of the relative position of the peak (from 0 to 1) on the variance of the peak.

Units that fired at least two action potentials in all the bursts in a recording were defined as backbone units. For murine organoids and cortical slices, a threshold of 80% and 90% of bursts was used, respectively, because only a small fraction of units had at least two action potentials in all bursts (Supplementary Fig. 2a). A backbone unit sequence was defined by ordering all backbone units based on their median FR peak time. For each sample, the burst backbone period was defined as the average FR peak time of the earliest backbone unit until the average FR peak time of the latest backbone unit in the sequence. For different plotting purposes, the backbone period was rescaled from 0 to 1 and data per organoid were overlaid and averaged over the rescaled backbone period for comparison.

Burst-to-burst FR correlations

For each unit, the FR was recomputed after removing all spikes that fell outside of the burst windows. Next, this FR was selected from −250 ms to 500 ms relative to each individual burst peak and a cross-correlation was computed for the unit FR between each pair of bursts for each individual unit (using the built-in MATLAB function 'xcorr' with maxlag = 10 ms and normalization = 'coeff'). Only bursts with at least two detected action potentials and units with at least two spikes in at least 30% of all bursts were considered for this analysis. Afterwards, the average over the maximum correlations for all the burst pairs with at least two detected action potentials was computed per unit, yielding the burst-to-burst correlation. The same computations were performed on 100 different shuffled spike matrices and the results from the original spike matrices were normalized using the $(A - B)/(A + B)$ strategy, where A is the measured value and B is the averaged value computed over the 100 shuffled datasets.

In a separate analysis, burst-to-burst correlations were computed between bursts from two recordings from the same organoid slice at 4-h intervals. Average burst-to-burst correlations were computed for pairs of bursts within each of the two same recordings, as well as for pairs of bursts where one burst came from the recording at 0 h and the other burst from the recording at 4 h.

Pairwise FR correlations

Using the same FR computed after removing spikes outside burst windows, cross-correlations were computed between each pair of units (using the built-in MATLAB function 'xcorr' with maxlag = 350 ms and normalization = 'coeff', a maxlag of 350 ms was chosen because the median backbone period over all samples except the murine primary cultures was 348 ms). The rate for the whole recording was used. The maximum correlation values for each unit pair were compared between pairs of backbone units, pairs of one backbone and one nonrigid unit and pairs of nonrigid units. The same computations were performed on 100 different shuffled spike matrices and the results from the original spike matrices were normalized using the $(A - B)/(A + B)$ strategy, where A is the measured value and B is the averaged value computed over the 100 shuffled datasets. In addition, for all pairs of backbone units, the lag time corresponding to the maximum correlation value was compared to the average absolute lag time over all shuffled datasets for the same unit pair.

Burst similarity score

At every frame relative to the burst peak, a vector containing the FRs for each unit was obtained. For every pair of bursts, the cosine similarity was computed between the vectors from the two different bursts. This yielded a matrix with pairwise burst similarity values at every frame relative to the burst peak. The average of this matrix was defined to be the burst similarity score for that relative frame. This score was computed for each frame from the earliest burst start time (relative to the burst peak across all bursts) to the latest burst end time (also relative to the burst peak across all bursts). The same computations were performed on the spike matrices after shuffling.

Besides computing the burst similarity score over all units, burst similarity scores were also computed for only a subset of units. In the first case, these subsets consisted of all backbone units and all nonrigid units, respectively. Subsequently, at each frame, the burst similarity score distribution for all burst pairs was compared using a paired sample, two-sided *t* test (using the built-in MATLAB function *t* test). In the second case, these subsets consisted of units with an average correlation value ('Pairwise FR correlations') in the top/bottom *i*th percentile, where *i* ranged from 20 to 95. Subsequently, the difference between the top and bottom *i*th percentile was quantified for this range as the sum of the burst similarity score over all frames in the backbone period. This was done to assess the burst similarity based only on highly/lowly correlated units. Similarly, the burst similarity score distribution for all burst pairs was compared between the top/bottom 20% of units and all units using a paired sample, two-sided *t* test.

PCA manifold analysis

The spike-rate matrix of an organoid with n units can be interpreted as a set of points in n dimensional space, where each axis holds the spike-rate trajectory of a specific unit. The PCs of this system are

the directions in this space that capture the majority of the dataset's variance. A dimensionality reduction is achieved by linearly projecting the dataset onto these PCs. This transformation collapses the n dimensional system to p dimensions where $p < n$, while preserving the dominant patterns exhibited by the system. For this analysis, PCs were computed via Eigen-decomposition of the covariance matrix, as discussed further below.

Before the dimensionality reduction step, the FR data were normalized for each unit individually using the z-score method, which centers the data around zero mean and unit s.d. The dimensionality reduction was performed on the following three separate selections of units: all units, backbone units only and nonrigid units only.

The cumulative sum of the variance explained per PC was computed for the PCs ordered from high variance to low. For each recording, the results for all units were subtracted from the results for backbone units only and nonrigid units only. Negative values mean that the cumulative sum of the variance explained by all units is larger than for the subset of units and positive values mean that the cumulative sum of the variance explained by all units is smaller.

Furthermore, the sum of the variance explained by the first three PCs was computed and divided by the summed explained variance of the first X PCs, where X is the lowest number of total PCs from the three selections—all units, backbone and nonrigid. This was done to account for differences in the total number of PCs per selection. This value was computed for the original data and for 100 different shuffled spike matrices and the results from the original spike matrices were normalized using the $(A - B)/(A + B)$ strategy, where A is the measured value and B is the averaged value computed over the 100 shuffled datasets. These scores were compared between the three selections and between the different model types as described in 'Statistical analyses for model comparisons'.

Randomized recording

Randomization of single-unit spike times was performed based on the methods discussed in refs. 38,69 to preserve each neuron's mean FR as well as the population-averaged FR distribution. This is necessary to avoid trivial differences that would arise simply by changes in the mean FR of a neuron. Briefly, whenever analyses were performed on a randomized recording, the randomization was done as follows (unless stated otherwise): two separate units, A and B, were selected and two separate frames, 1 and 2, were selected where A but not B fired in frame 1 and B but not A fired in frame 2. Next, the spikes from unit A to unit B were switched between frames 1 and 2. The resulting spike matrix still has an equal number of spikes per unit (same average FR) and an equal number of spikes per frame (same population rate). This shuffling procedure was performed five times more often than there were spikes in the spike matrix, resulting in each spike being shuffled an average of ten times. This method was applied to produce 100 different shuffled spike matrices per original recording.

Statistical analyses for model comparisons

Statistical modeling was carried out in the R environment (version 4.2.1). Nested data were analyzed with linear mixed-effects models ('lmer' function of the lme4 R package[70]) with 'organoid' or 'unit ID' as random effect. Non-nested data were analyzed with linear models ('lm' function). Right-skewed and heavy-tailed data were log-transformed and analyzed with a linear model. Statistical significance for linear mixed-effects models was computed with the lmerTest R package[71] and the summary (type III sums of squares) R function. Statistical significance for linear models was computed with the summary R function. When possible, model selection was performed according to the experimental design. When this was not possible, models were compared using the 'compare_performance' function of the performance R package[72], and model choice was based on a holistic comparison of AIC, BIC, RMSE and R2. Model output was plotted with the 'plot_model' (type='pred') function of the sjPlot R package[73]. A total of 95% confidence intervals were computed using the 'confint' R function. Post hoc analysis was carried out using the 'emmeans' and 'emtrends' functions of the 'emmeans' R package.

Reporting summary

Further information on research design is available in the Nature Portfolio Reporting Summary linked to this article.

Data availability

The data supporting the findings of this study are available within the article and its supplementary information. Raw and curated electrophysiology recordings can be found here https://dandiarchive.org/dandiset/001603. scRNA-seq data have been deposited and are publicly available in the NCBI Gene Expression Omnibus (http://www.ncbi.nlm.nih.gov/geo) with accession GSE290330.

Code availability

Spike sorting was performed in Python 3.6 using SpikeInterface 0.13.0 and previously published[63], which can be found at https://github.com/SpikeInterface/spikeinterface. Custom code for electrophysiology analysis is available at https://github.com/braingeneers/Protosequences

References

63. Buccino, A. P. et al. SpikeInterface, a unified framework for spike sorting. *eLife* **9**, e61834 (2020).
64. Pachitariu, M., Steinmetz, N., Kadir, S., Carandini, M. & Harris, K. Fast and accurate spike sorting of high-channel count probes with KiloSort. In *Proc. Advances in Neural Information Processing Systems* (eds Lee, D. et al.) 4455–4463 (Curran Associates, Inc., 2016).
65. Hill, D. N., Mehta, S. B. & Kleinfeld, D. Quality metrics to accompany spike sorting of extracellular signals. *J. Neurosci.* **31**, 8699–8705 (2011).
66. Romero, J. C. et al. Oligodendrogenesis and myelination tracing in a CRISPR/Cas9-engineered brain microphysiological system. *Front. Cell. Neurosci.* **16**, 1094291 (2023).
67. Bartram, J. et al. Cortical up states induce the selective weakening of subthreshold synaptic inputs. *Nat. Commun.* **8**, 665 (2017).
68. Holt, G. R., Softky, W. R., Koch, C. & Douglas, R. J. Comparison of discharge variability in vitro and in vivo in cat visual cortex neurons. *J. Neurophysiol.* **75**, 1806–1814 (1996).
69. Okun, M. et al. Population rate dynamics and multineuron firing patterns in sensory cortex. *J. Neurosci.* **32**, 17108–17119 (2012).
70. Bates, D., Mächler, M., Zurich, E., Bolker, B. M. & Walker, S. C. Fitting linear mixed-effects models using lme4. *J. Stat. Softw.* **67**, 1–48 (2015).
71. Kuznetsova, A., Brockhoff, P. B. & Christensen, R. H. B. lmerTest package: tests in linear mixed effects models. *J. Stat. Softw.* **82**, 1–26 (2017).
72. Lüdecke, D., Ben-Shachar, M., Patil, I., Waggoner, P. & Makowski, D. Performance: an R package for assessment, comparison and testing of statistical models. *J. Open Source Softw.* **6**, 3139 (2021).
73. Long, J. A. jtools: analysis and presentation of social scientific data. *J. Open Source Softw.* **9**, 6610 (2024).

Acknowledgements

We would like to thank the members of the Braingeneers consortium for helpful discussions and D. Haussler for insightful comments. We would also like to thank members of the UC Santa Cruz Genomics Institute for helping with computing resources, in particular D. Parks for assistance with archiving the neurophysiology data. This study was supported by the National Science Foundation (NSF) Emerging Frontiers in Research and Innovation under award (NSF 2515389 to T.S.),

UC Santa Cruz Baskin Engineering Seed Grant (to T.S.), Schmidt Futures Foundation (SF857 to M.T.), National Human Genome Research Institute under award (1RM1HG011543 to M.T.), German Research Foundation FOR5159 TP1 (437610067 to I.L.H.-O.), European Research Council advanced grant 'neuroXscales' (694829 to A.H.), Swiss NSF project (205320_188910/1 to A.H.), National Institutes of Health (NIH; T32 ES007141 to D.-M.A.E.D.) and International Foundation for Ethical Research (to D.-M.A.E.D.), Hopkins Discovery and Johns Hopkins SURPASS (to L.S.), John Douglas French Alzheimer's Foundation (to K.S.K.), NIH BRAIN Initiative (R01NS118442 to K.B.H.) and National Institute of Mental Health grant (1U24MH132628 to M.A.M.-R.). Through the National Research Platform, this work was supported in part by NSF awards (CNS-1730158, ACI-1540112, ACI-1541349, OAC-1826967, OAC-2112167, CNS-2100237 and CNS-2120019), the University of California Office of the President and the University of California San Diego's California Institute for Telecommunications and Information Technology/Qualcomm Institute.

Author contributions

T.S. designed, conceived and supervised the study. M.C., I.L.H.-O., K.B.H. and K.S.K. offered numerous suggestions and comments. T.v.d.M., A.S. and M.C. performed computational analysis and statistics on electrophysiology recordings. J.B. and T.G. performed extracellular recordings on acute brain slices under the supervision of A.H. S.H., G.A.K., H.E.S., C.D. and S.M. cultured mouse brain organoids and performed electrophysiology measurements under the supervision of T.S. and M.A.M.-R. S.H., G.A.K. and H.E.S. performed single-cell RNA sequencing and immunohistochemistry of mouse organoids under the supervision of M.A.M.-R., B.M.C. and T.S. C.R.K.H. performed additional immunohistochemistry and fluorescence microscopy under the supervision of T.S. S.H., H.E.S. and J.G.-F. performed analysis on single-cell RNA sequencing data from mouse organoids under the supervision of M.A.M.-R. and B.M.C. D.-M.A.E.D., J.L. and M.S. performed electrophysiology measurements and bulk RNA sequencing of additional human brain organoids under the supervision of L.S. A.D., Z.Z. and M.L. performed additional electrophysiology analysis under the supervision of T.v.d.M., L.R.P. and P.K.H. K.B.-N. performed computational analysis under the supervision of K.B.H. A.L.M. and J.G. contributed to spike sorting and archiving neurophysiology datasets under the supervision of T.S. and M.T. T.S. wrote the first draft of the paper. M.C., I.L.H.-O., K.B.H., T.v.d.M. and K.S.K. provided valuable edits to subsequent drafts, and all authors discussed the results and commented on the paper.

Competing interests

The authors declare no competing interests.

Additional information

Extended data is available for this paper at https://doi.org/10.1038/s41593-025-02111-0.

Supplementary information The online version contains supplementary material available at https://doi.org/10.1038/s41593-025-02111-0.

Correspondence and requests for materials should be addressed to Tal Sharf.

Peer review information *Nature Neuroscience* thanks Giorgia Quadrato and the other, anonymous, reviewer(s) for their contribution to the peer review of this work.

https://doi.org/10.1038/s41593-025-02111-0

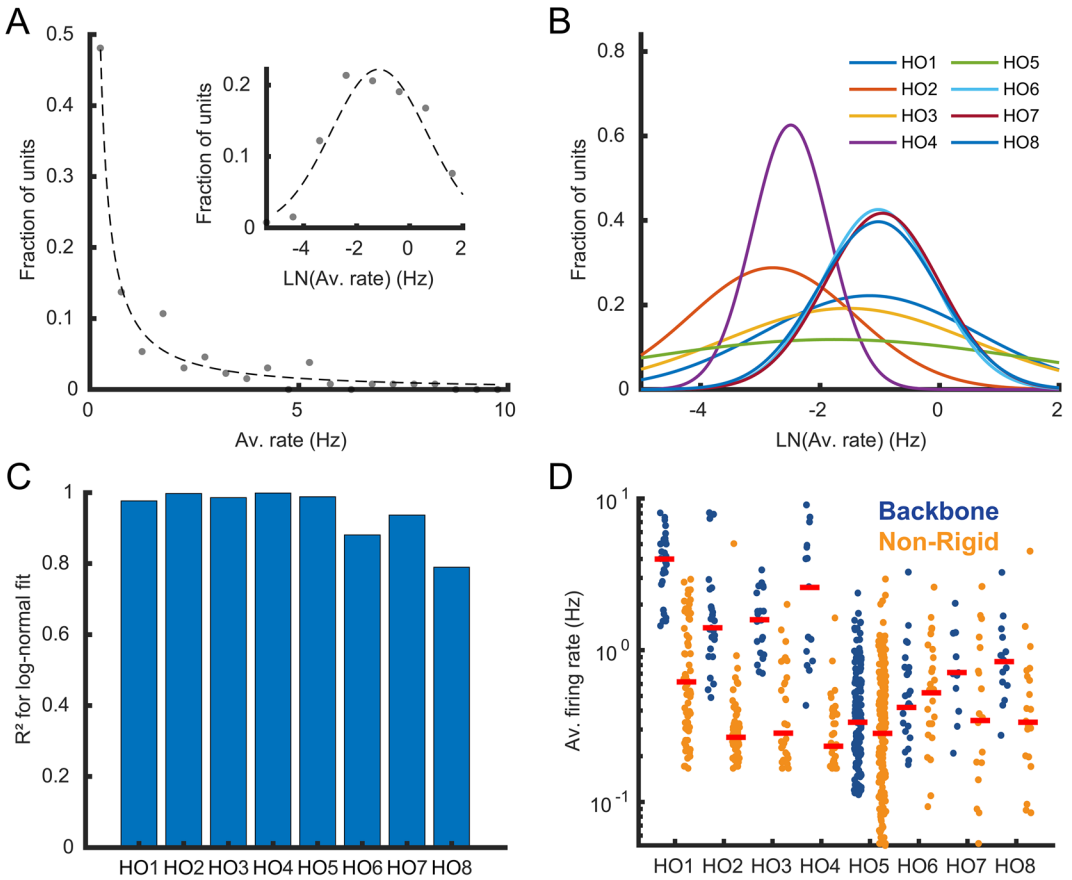

Extended Data Fig. 1 | Backbone units occupy the tail of skewed firing rate distributions. a, A histogram of the distribution of average firing rates for all units in organoid 1. The majority of units have low average firing rates, while a long tail in the distribution contains a small subset of units with high average firing rates. A lognormal distribution is fitted to the histogram. The inset shows the histogram for the logarithm of the average firing rates of the same organoid. A normal distribution is fitted to the histogram. **b**, Normal distributions fit to the logarithm of the average firing rate per unit for the 8 different organoids. **c**, The R^2 values for the fitted normal distributions shown in **b**. $R^2 = 0.97 \pm 0.04$ (mean ± s.d.) across the 8 human brain organoids. Backbone neurons alone are not well described by a lognormal distribution. R^2 values are 0.45 ± 0.30 across the 8 human brain organoids. **d**, The distribution of average firing rates per organoid for backbone and non-rigid units separated. Red bars mark the distribution medians. The backbone units populate the tail of the skewed average firing rate distributions in all organoids. See Fig. 7a for statistical comparisons.

https://doi.org/10.1038/s41593-025-02111-0

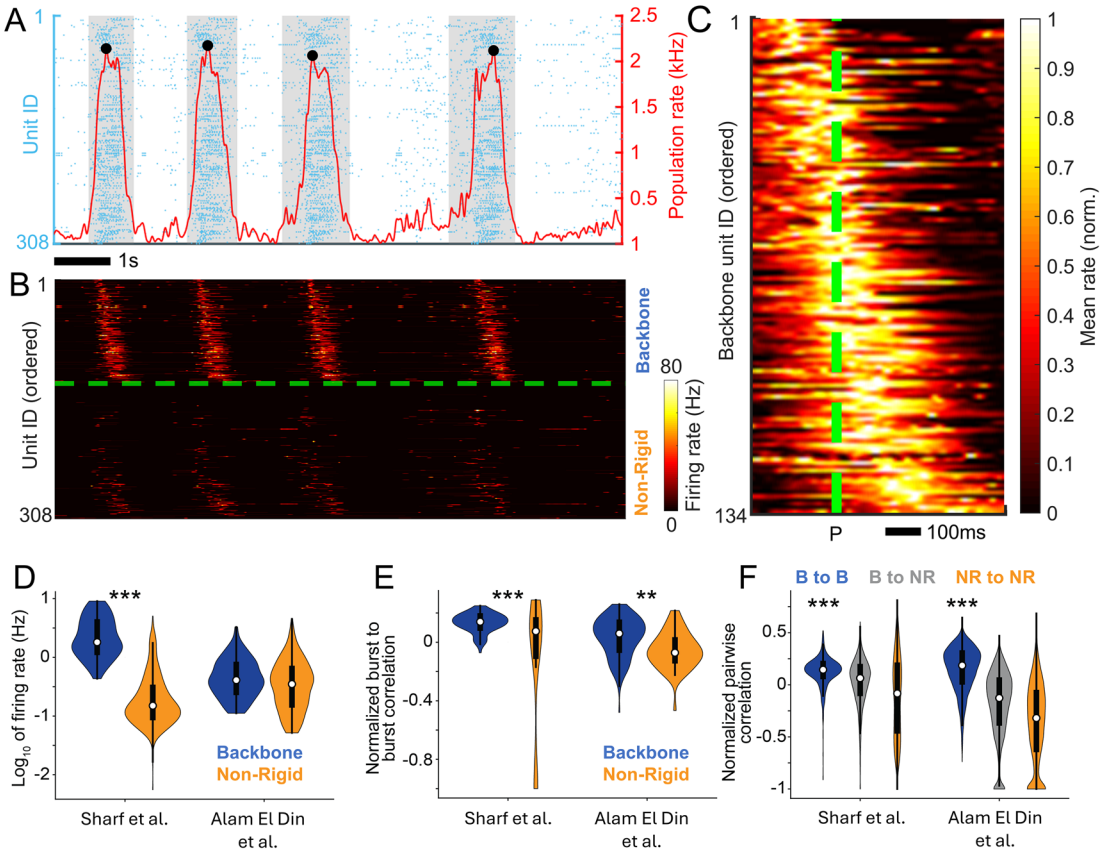

Extended Data Fig. 2 | Reproducible firing patterns in human brain organoids. **a**, Raster plot visualization of single-unit spiking (blue dots) measured across the surface of a human brain organoid slice from ref. 27 (HO5), positioned on top of the same Maxwell Biosystems microelectrode array as used for the organoid recordings included in the main Figs. 1–5. The population firing rate is shown by the red solid line. Population bursts are marked by sharp increases in the population rate. Burst peak events are denoted by local maxima (black dots) that exceed 4× r.m.s. fluctuations in the population rate. The shaded gray regions denote the burst duration window as defined by the time interval in which the population rate remains above 10% of its peak value in the burst. **b**, The instantaneous firing rate of single-unit activity from **a** after reordering. The backbone units are plotted above the dashed line, while non-rigid units are plotted below the dashed line. In each category, units are ordered based on their median firing rate peak time relative to the burst peak, considered over all bursts in the recording. **c**, The average burst peak-centered firing rate measured across all burst events for the example recording of which part is shown in **a**. The burst peak is indicated by the dotted line. The unit order is the same as **b**. Please note the progressive increase in the firing rate peak time relative to the burst peak, as well as a spread in the active duration for units having their peak activity later in the burst. The average firing rate is normalized per unit to aid in visual clarity. **d**, The distributions of the log of the average firing rate per unit, separated for backbone and non-rigid units. All units from the four recordings mentioned in ref. 22 are pooled together and all units from the four recordings mentioned in ref. 27 are pooled together ($P < 10^{-20}$ and $P = 0.40$, respectively, two-sided linear mixed-effect model, $n = 4$ organoids each). **e**, The distributions of the average burst-to-burst correlations per unit after average rate normalization, separated for backbone and non-rigid units. All units from the four recordings mentioned in ref. 22 are pooled together and all units from the four recordings mentioned in ref. 27 are pooled together. Please note the significant difference between backbone and non-rigid units present for both sets of recordings ($P = 1 \times 10^{-10}$ and $P = 0.0092$, respectively, two-sided linear mixed-effect model, $n = 4$ organoids each). **f**, The distributions of the pairwise correlations per unit pair after average rate normalization, separated for backbone pairs, backbone and non-rigid combinations and non-rigid pairs. All unit pairs from the four recordings mentioned in ref. 22 are pooled together and all unit pairs from the four recordings mentioned in ref. 27 are pooled together. Please note that only the normalized correlation for backbone pairs are significantly larger than 0 for both sets of recordings ($P = 0.0001$, 0.145 and 1; $P = 7 \times 10^{-11}$, 1 and 1, respectively), one-sided linear mixed-effect model, $n = 4$ organoids each).

https://doi.org/10.1038/s41593-025-02111-0

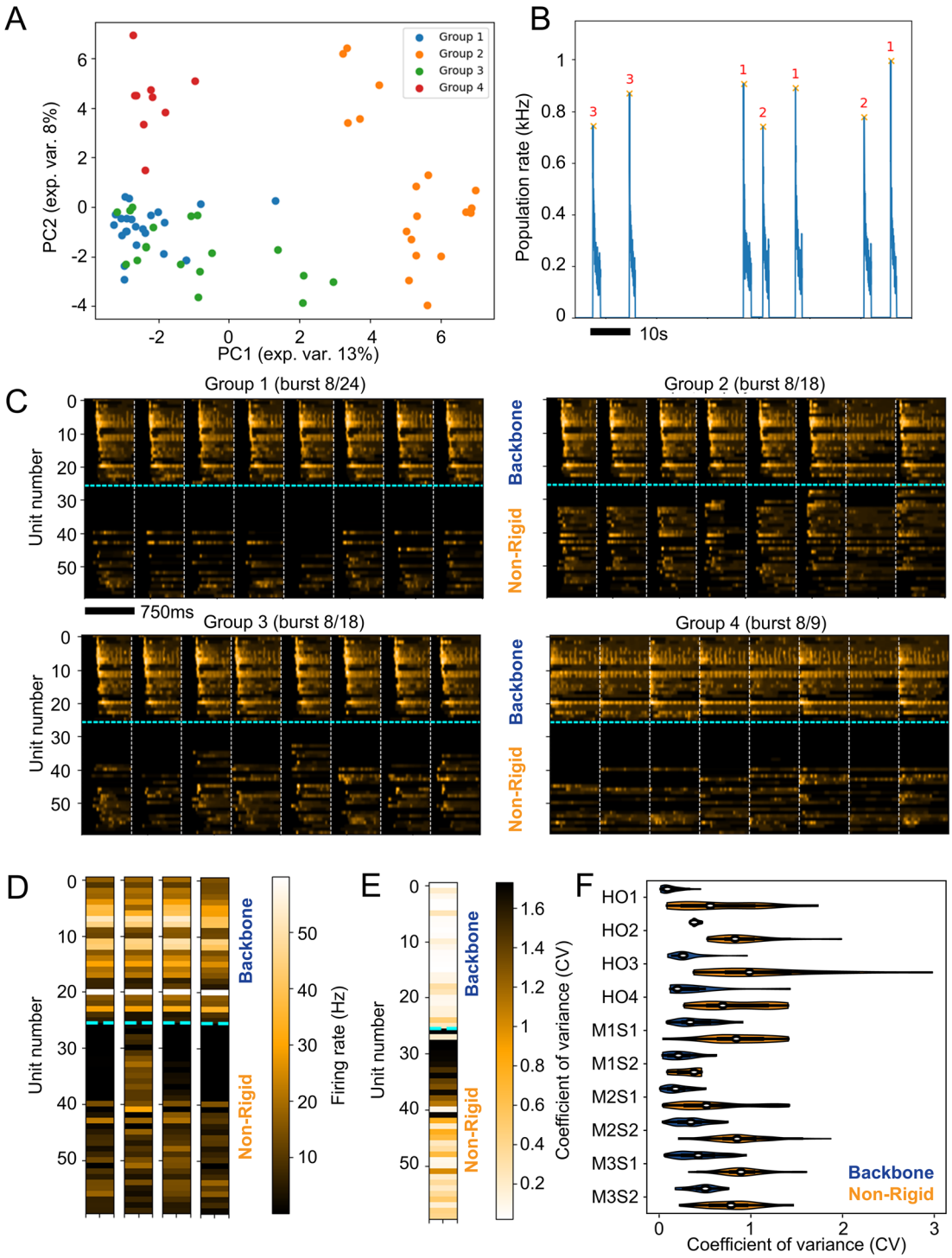

Extended Data Fig. 3 | Burst clustering distinguishes non-rigid from backbone unit variability. a, Pairwise firing rate correlations per burst (computed over a window ranging from −250 ms until 500 ms relative to the burst peak) projected onto the first two principal components, labeled by the identified clusters, show a clear separation between different burst clusters. The results, for example, recording Or5, are shown. **b**, The population rate for a snippet of the recording for Or5 covering several bursts labeled by their cluster. **c**, Firing rates per unit for 8 different example bursts per cluster. **d**, The average firing rate per unit for the different detected burst clusters. **e**, A selection of non-rigid units is most variable in their activity between the different burst clusters as reflected by a higher CV score for their firing rate in the different burst clusters (CV scores are computed per row for the 4 columns shown in **d**). **f**, The CV scores for the firing rate over the different burst clusters are significantly higher for non-rigid units compared to backbone units ($P \leq 10^{-20}$ for difference between backbone and non-rigid, two-sided linear mixed-effect model).

https://doi.org/10.1038/s41593-025-02111-0

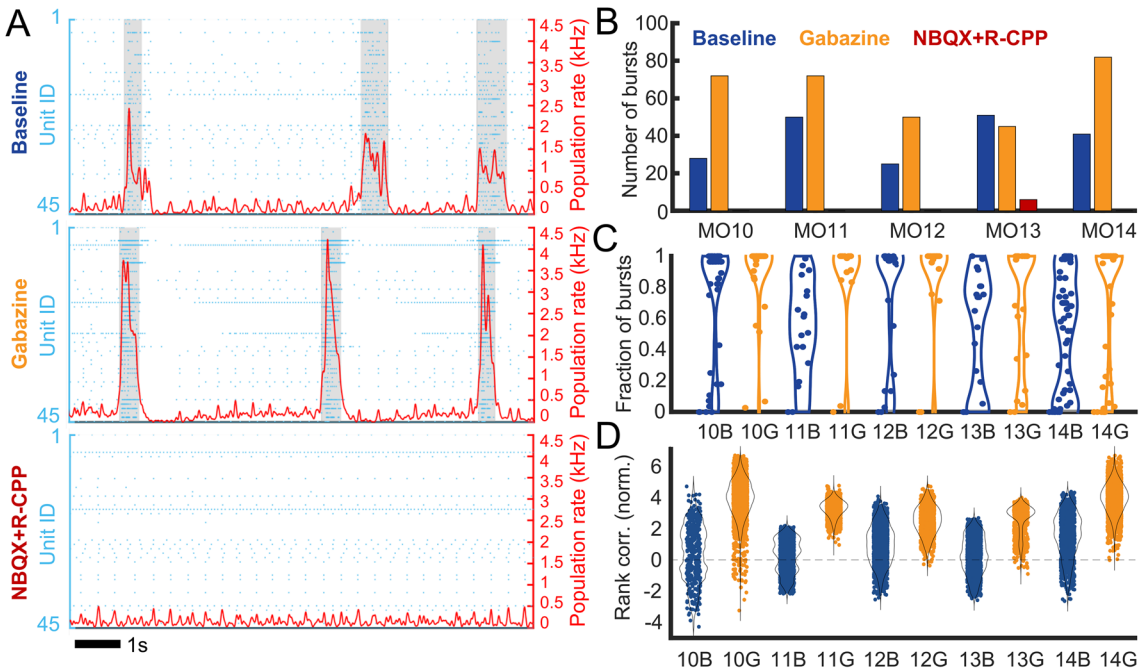

Extended Data Fig. 4 | Pharmacological modulation of excitatory and inhibitory signaling impacts bursts and sequences. a, Raster plot visualization of single-unit spiking (blue dots) measured across the surface of a murine organoid (MO10), positioned on top of the same type of microelectrode array as used for the recordings included in the main figures. The population firing rate is shown by the red solid line. Population bursts are marked by sharp increases in the population rate. The shaded gray regions denote the burst duration window as defined by the time interval in which the population rate remains above 10% of its peak value in the burst. Top: baseline recording. Middle: recording of the same organoid using the same electrode configuration, after treatment with 10 µM gabazine to inhibit inhibitory signaling by blocking $GABA_A$ receptors. Bottom: recording of the same organoid slice using the same electrode configuration, after blocking AMPA and NMDA receptors with bath application of NBQX (10 µM) and R-CPP (20 µM) to inhibit components of excitatory synaptic transmission. **b**, Number of detected population bursts for 5 different murine organoids (MO10-14) under baseline conditions, after treatment with gabazine and after treatment with NBQX and R-CPP. Please note that bursting disappears after NBQX and R-CPP treatment reflected as a significant decrease in bursting compared to baseline conditions ($P < 0.001$, two-sided linear mixed-effect model). Meanwhile, the number of bursts increase after gabazine treatment ($P < 0.05$, two-sided linear mixed-effect model). **c**, Fraction of bursts in which a unit fires at least 2 spikes for the 5 different murine organoids under baseline conditions compared to the gabazine treatment. The fraction of bursts in which units are active increases significantly after gabazine treatment ($P < 10^{-7}$, two-sided linear mixed-effect model). **d**, Normalized Spearman rank-order correlations comparing the sequential order of backbone sequences for all burst pairs of 5 different murine organoids (MO10-14) under baseline conditions and after treatment with gabazine. Correlation scores are z-scored relative to shuffled spike matrices such that values above 0 indicate a more consistent backbone sequence than the shuffled data. There is a significant increase in backbone sequence order similarity after treatment with gabazine ($P < 10^{-20}$, two-sided linear mixed-effect model).

https://doi.org/10.1038/s41593-025-02111-0

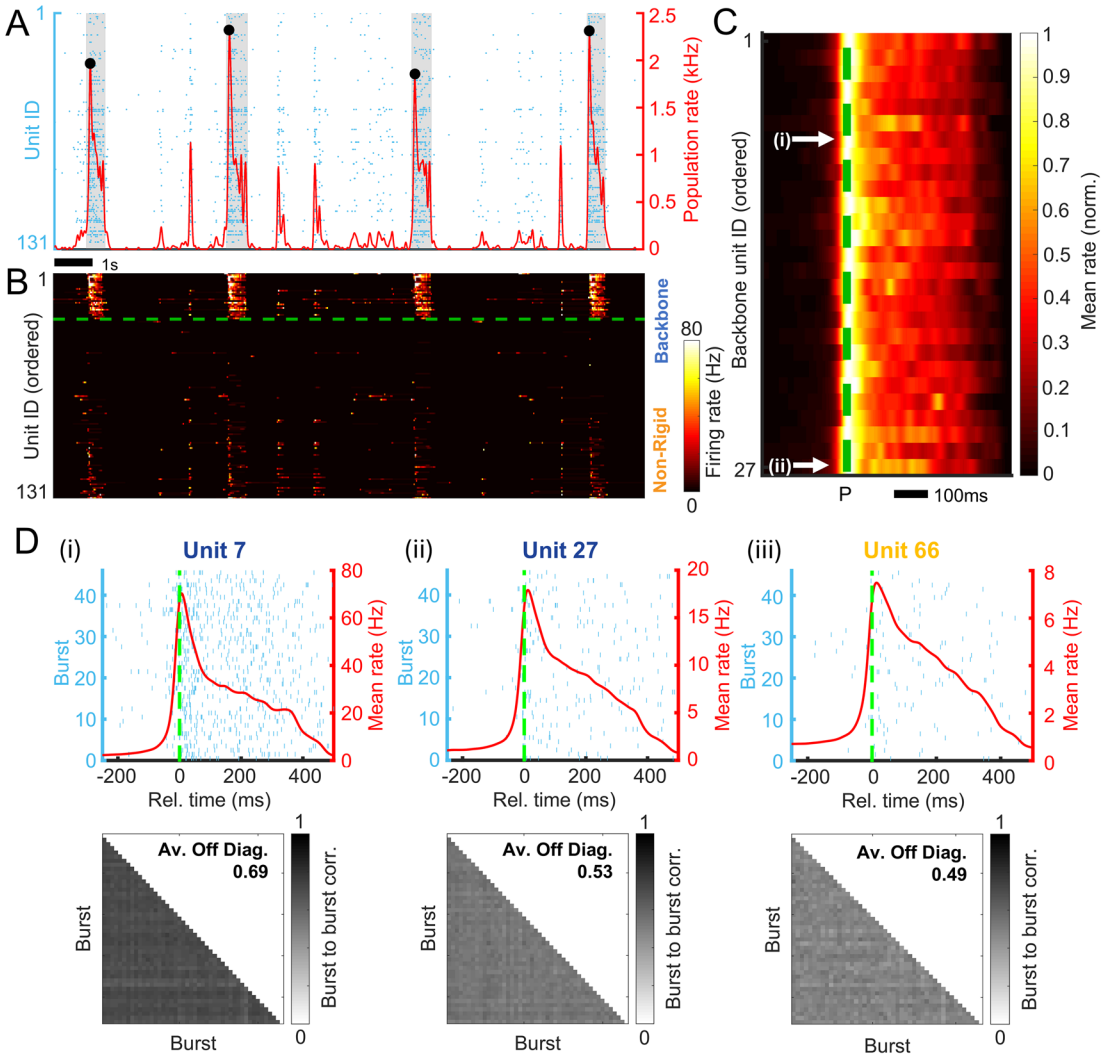

Extended Data Fig. 5 | Sequential activations and burst-to-burst similarity are not present after shuffling. a, Same raster plot visualization as Fig. 1a after shuffling. The population firing rate remains the same after shuffling and is shown by the red solid line. Population bursts exist in the same frames after shuffling and are denoted by local maxima (black dots) that exceed 4× r.m.s. fluctuations in the population rate. The burst duration windows remain the same after shuffling and are marked by the shaded gray regions, which denote the interval in which the population rate remains above 10% of its peak value in the burst. The average firing rate per unit remains the same after shuffling. **b**, Same instantaneous firing rate visualization as Fig. 2b. The same ordering is used as in Fig. 2b. **c**, Same average burst peak-centered firing rate visualization as Fig. 2c after shuffling. The burst peak is indicated by the dotted line. The unit order is the same as Fig. 2c. Please note that the progressive increase in the firing rate peak time relative to the burst peak, as well as a spread in the active duration for units having their peak activity later in the burst are not present anymore after shuffling. The average firing rate is normalized per unit to aid in visual clarity. **d**, Same burst-peak-centered spike times and pairwise burst-to-burst correlations as in Fig. 2d after shuffling. For (i) and (ii), the consistent firing patterns relative to the burst peak as exemplified in Fig. 2d are not present anymore and the average burst-to-burst correlation scores have decreased from 0.96 to 0.69 and from 0.82 to 0.53, respectively. Meanwhile, the average burst-to-burst correlation for the non-rigid unit exemplified in (iii) decreased from 0.51 to 0.49.

https://doi.org/10.1038/s41593-025-02111-0

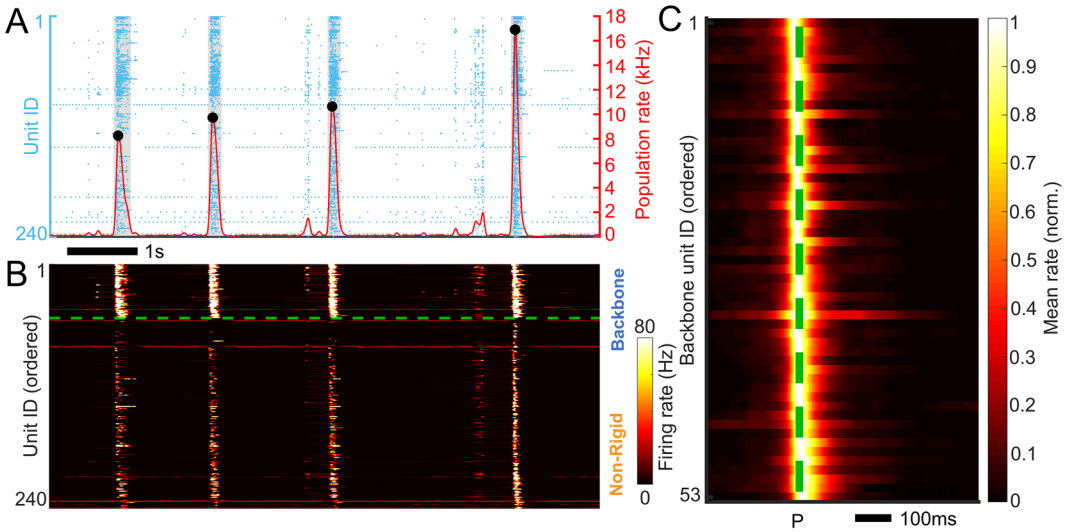

Extended Data Fig. 6 | Intrinsic activity in murine primary cultures resembles organoids after shuffling. a, Raster plot visualization of single-unit spiking (blue dots) measured across a 2D murine primary culture from ref. 28 (Pr1) recorded on a high-density microelectrode array. The population firing rate is shown by the red solid line. Population bursts are marked by sharp increases in the population rate. Burst peak events are denoted by local maxima (black dots) that exceed 4× r.m.s. fluctuations in the population rate. The shaded gray regions denote the burst duration window as defined by the time interval in which the population rate remains above 10% of its peak value in the burst. **b**, The instantaneous firing rate of single-unit activity from **a** after reordering. The backbone units are plotted above the dashed line, while non-rigid units are plotted below the dashed line. In each category, units are ordered based on their median firing rate peak time relative to the burst peak, considered over all bursts in the recording. **c**, The average burst peak-centered firing rate measured across all burst events for the example recording of which part is shown in **a**. The burst peak is indicated by the dotted line. The unit order is the same as **b**. Please note that the progressive increase in the firing rate peak time relative to the burst peak, as well as a spread in the active duration for units having their peak activity later in the burst are not present in the murine primary recording, similar to the organoid data after shuffling as shown in Extended Data Fig. 5. The average firing rate is normalized per unit to aid in visual clarity.

https://doi.org/10.1038/s41593-025-02111-0

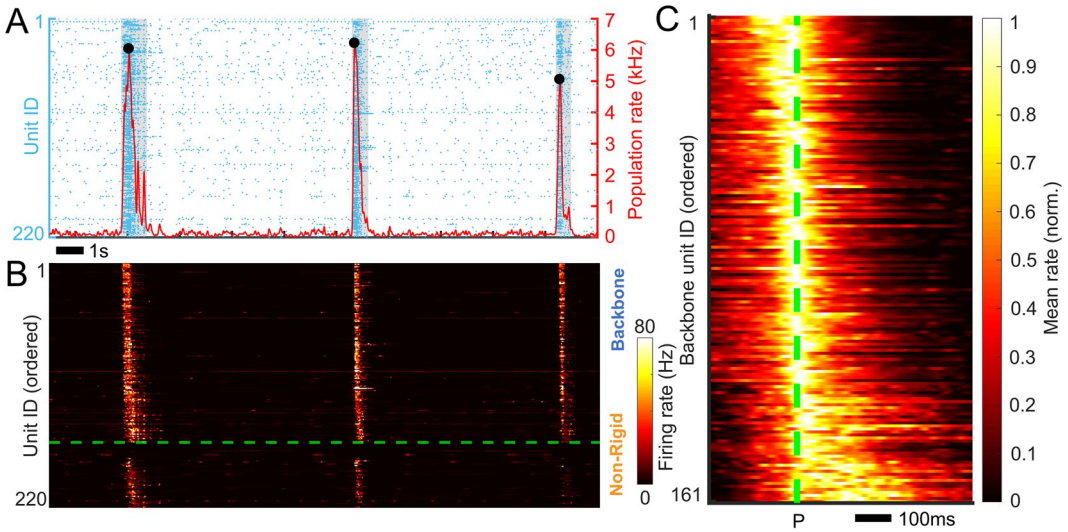

Extended Data Fig. 7 | Consistent results in brain slices from different animals. **a**, Raster plot visualization of single-unit spiking (blue dots) measured across the surface of a murine neonatal cortical slice from a different animal (M3S1) dissected at P13, positioned on top of the same type of microelectrode array as used for the recordings included in main Fig. 6. The population firing rate is shown by the red solid line. Population bursts are marked by sharp increases in the population rate. Burst peak events are denoted by local maxima (black dots) that exceed 4× r.m.s. fluctuations in the population rate. The shaded gray regions denote the burst duration window as defined by the time interval in which the population rate remains above 10% of its peak value in the burst. **b**, The instantaneous firing rate of single-unit activity from **a** after reordering. The backbone units are plotted above the dashed line, while non-rigid units are plotted below the dashed line. In each category, units are ordered based on their median firing rate peak time relative to the burst peak, considered over all bursts in the recording. **c**, The average burst peak-centered firing rate measured across all burst events for the example recording of which part is shown in **a**. The burst peak is indicated by the dotted line. The unit order is the same as **b**. Please note the progressive increase in the firing rate peak time relative to the burst peak, as well as a spread in the active duration for units having their peak activity later in the burst. The average firing rate is normalized per unit to aid in visual clarity.

https://doi.org/10.1038/s41593-025-02111-0

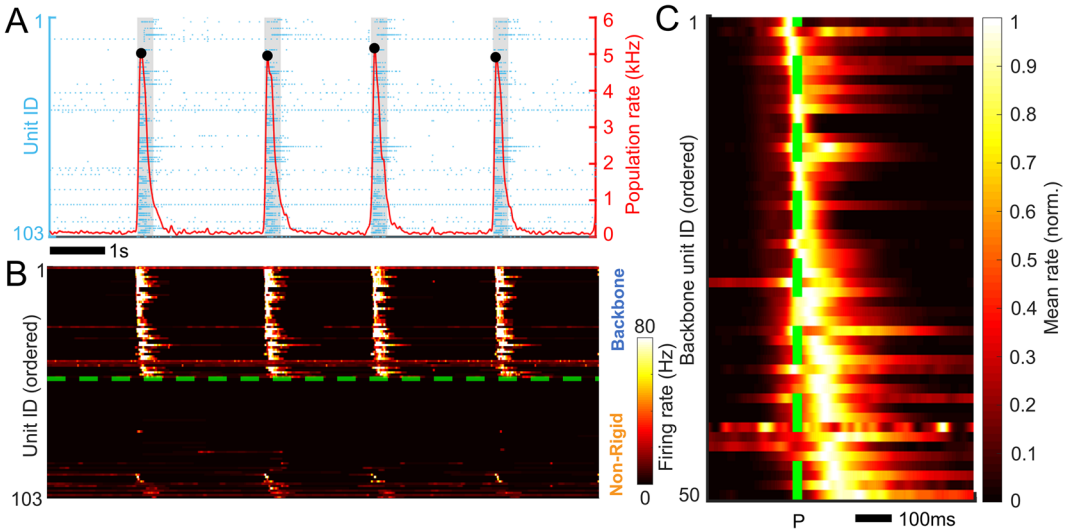

Extended Data Fig. 8 | Backbone sequences observed during spontaneous population bursts in murine cortical organoids. a, Raster plot visualization of single-unit spiking (blue dots) measured across the surface of a murine organoid (MO1) recorded at 42 DIV, positioned on top of the same type of microelectrode array as used for the recordings included in the main figures. The population firing rate is shown by the red solid line. Population bursts are marked by sharp increases in the population rate. Burst peak events are denoted by local maxima (black dots) that exceed 4x-r.m.s. fluctuations in the population rate. The shaded gray regions denote the burst duration window as defined by the time interval in which the population rate remains above 10% of its peak value in the burst. **b**, The instantaneous firing rate of single-unit activity from panel **a** after reordering. The backbone units are plotted above the dashed line, while non-rigid units are plotted below the dashed line. In each category, units are ordered based on their median firing rate peak time relative to the burst peak, considered over all bursts in the recording. **c**, The average burst peak-centered firing rate measured across all burst events for the example recording of which part is shown in **a**. The burst peak is indicated by the dotted line. The unit order is the same as **b**. Please note the progressive increase in the firing rate peak time relative to the burst peak, as well as a spread in the active duration for units having their peak activity later in the burst. The average firing rate is normalized per unit to aid in visual clarity.

nature portfolio

Corresponding author(s): Tal Sharf

Last updated by author(s): Sep 15, 2025

Reporting Summary

Nature Portfolio wishes to improve the reproducibility of the work that we publish. This form provides structure for consistency and transparency in reporting. For further information on Nature Portfolio policies, see our Editorial Policies and the Editorial Policy Checklist.

Statistics

For all statistical analyses, confirm that the following items are present in the figure legend, table legend, main text, or Methods section.

n/a	Confirmed
☐	☒ The exact sample size (*n*) for each experimental group/condition, given as a discrete number and unit of measurement
☐	☒ A statement on whether measurements were taken from distinct samples or whether the same sample was measured repeatedly
☐	☒ The statistical test(s) used AND whether they are one- or two-sided *Only common tests should be described solely by name; describe more complex techniques in the Methods section.*
☐	☒ A description of all covariates tested
☐	☒ A description of any assumptions or corrections, such as tests of normality and adjustment for multiple comparisons
☐	☒ A full description of the statistical parameters including central tendency (e.g. means) or other basic estimates (e.g. regression coefficient) AND variation (e.g. standard deviation) or associated estimates of uncertainty (e.g. confidence intervals)
☐	☒ For null hypothesis testing, the test statistic (e.g. *F*, *t*, *r*) with confidence intervals, effect sizes, degrees of freedom and *P* value noted *Give P values as exact values whenever suitable.*
☒	☐ For Bayesian analysis, information on the choice of priors and Markov chain Monte Carlo settings
☒	☐ For hierarchical and complex designs, identification of the appropriate level for tests and full reporting of outcomes
☐	☒ Estimates of effect sizes (e.g. Cohen's *d*, Pearson's *r*), indicating how they were calculated

Our web collection on statistics for biologists contains articles on many of the points above.

Software and code

Policy information about availability of computer code

Data collection	MaxLab Live (version 19.2.19, 22.2.6, 22.2.8, 25.1.6.1), Maxwell Biosystems
Data analysis	MATLAB (MathWorks), Python, R; SpikeInterface 0.13.0 in Python (https://github.com/SpikeInterface); custom MATLAB (version 2018b), Python (version 3.6 and 3.11) and R (version 4.2.1) code for MEA analysis as described in methods is here: https://github.com/braingeneers/Protosequences.

For manuscripts utilizing custom algorithms or software that are central to the research but not yet described in published literature, software must be made available to editors and reviewers. We strongly encourage code deposition in a community repository (e.g. GitHub). See the Nature Portfolio guidelines for submitting code & software for further information.

Data

Policy information about availability of data

All manuscripts must include a data availability statement. This statement should provide the following information, where applicable:

- Accession codes, unique identifiers, or web links for publicly available datasets
- A description of any restrictions on data availability
- For clinical datasets or third party data, please ensure that the statement adheres to our policy

The data supporting the findings of this study are available within the article and its supplementary information. Raw and curated electrophysiology recordings can

be found here https://dandiarchive.org/dandiset/001603. scRNA-seq data have been deposited and are publicly available in the NCBI Gene Expression Omnibus (GEO; http://www.ncbi.nlm.nih.gov/geo) under accession GSE290330.

Research involving human participants, their data, or biological material

Policy information about studies with human participants or human data. See also policy information about sex, gender (identity/presentation), and sexual orientation and race, ethnicity and racism.

Reporting on sex and gender	N/A
Reporting on race, ethnicity, or other socially relevant groupings	N/A
Population characteristics	N/A
Recruitment	N/A
Ethics oversight	N/A

Note that full information on the approval of the study protocol must also be provided in the manuscript.

Field-specific reporting

Please select the one below that is the best fit for your research. If you are not sure, read the appropriate sections before making your selection.

☒ Life sciences ☐ Behavioural & social sciences ☐ Ecological, evolutionary & environmental sciences

For a reference copy of the document with all sections, see nature.com/documents/nr-reporting-summary-flat.pdf

Life sciences study design

All studies must disclose on these points even when the disclosure is negative.

Sample size	Sample size for organoid and primary culture recordings were determined by the data available in Sharf et al. and Alam El Din et al. Murine organoids were set by the number of available organoids. Acute murine slice recordings were set by the number of available pups.
Data exclusions	Due to intrinsic neurophysiological variability occurring during brain organoid development, organoids exhibited a range in the number of active spiking units. Organoids with less than 20 units were not considered for recordings in the murine, Sharf et al. and Alam El Din et al. data. In order to compare the same number of burst events across all samples the first x minutes of the recordings were used so each recording had a similar number of burst events.
Replication	All experiments were performed with sufficient biological replicates across biological models. Additionally, experimental approaches are documented with sufficient detail for precise replication.
Randomization	Single-unit spike times were randomized to preserve both each neuron's mean firing rate and the population-averaged firing rate distribution. The resulting spike matrix contained an equal number of spikes per unit (same average firing rate) and per frame (same population rate). For murine cortical brain slice experiments, neonatal pups of both sexes were selected at random, and slices from the somatosensory cortex were chosen randomly prior to acute electrophysiology. Murine cortical organoids were also selected randomly for electrophysiological recordings.
Blinding	Human and murine brain organoids and murine cortical slices were grown or prepared in separate laboratories, so sample collection could not be blinded. Data analyses were performed blind to the conditions of the experiments.

Reporting for specific materials, systems and methods

We require information from authors about some types of materials, experimental systems and methods used in many studies. Here, indicate whether each material, system or method listed is relevant to your study. If you are not sure if a list item applies to your research, read the appropriate section before selecting a response.

Materials & experimental systems

n/a	Involved in the study
☐	☒ Antibodies
☐	☒ Eukaryotic cell lines
☒	☐ Palaeontology and archaeology
☐	☒ Animals and other organisms
☒	☐ Clinical data
☒	☐ Dual use research of concern
☒	☐ Plants

Methods

n/a	Involved in the study
☒	☐ ChIP-seq
☒	☐ Flow cytometry
☒	☐ MRI-based neuroimaging

Antibodies

Antibodies used

Primary antibodies used for murine organoids: rabbit anti-Map2 (Proteintech # 17490-1-AP, 1:2000); mouse anti-Pax6 (BD Biosciences # 561462, 1:100); rabbit anti-Nkx2.1 (Abcam # ab76013, 1:400); rat anti-Ctip2 (Abcam # ab18465, 1:250); rabbit anti-Brn2 (Thermofisher # PA530124, 1:400); anti-Gaba (Thermo Fisher Scientific # PA5-32241, 1:375). Secondary antibodies were of the Alexa series (Thermo Fisher Scientific), used at a concentration of 1:750. Nuclear counterstain was performed using 1.0 µg/ml Hoechst 33342 (Thermofisher # H1399)

Primary antibodies used for human organoids: mouse anti-Gephyrin(Synaptic Systems #147 011, Monoclonal Mouse IgM Clone mAb7a ,1:1000); chicken anti-MAP2 (Invitrogen #PA1-10005,1:5000), rabbit anti-GFAP (Dako #Z0334, 1:400); mouse anti-O4 (R&D #MAB1326,Monoclonal Mouse IgM Clone # O4, 1:200)

Validation

Antibodies used for murine cortical organoids:
MAP2 (Proteintech 17490-1-AP): Microtubule-associated protein 2 (MAP2) is a tubulin binding protein regulating the spacing and stability of microtubules and contributing to elongation of dendrites. MAP2 has multiple isoforms that arise from alternative splicing (PMID: 3121794, 7854050, and 10383434). They are classified into two groups - MAP2A and MAP2B, which are known as high molecular weight (HMW) isoforms, run as ~280 kDa species, while low molecular weight (LMW) isoforms MAP2C and MAP2D are around ~70 kDa. MAP2 proteins are heavily phosphorylated, which contributes to a large discrepancy between their predicted and observed molecular weight in SDS-PAGE (220 vs 280 kDa for HMW forms). In neurons, MAP2 proteins are found in the cell body and dendrites, where they associate with microtubules, while they can also be present in the nuclei of testicular cells.
Tested Reactivity: human, mouse, rat
Host / Isotype: Rabbit / IgG
Class: Polyclonal
Calculated Molecular Weight: 200 kDa
Observed Molecular Weight: 280 kDa, 70-85 kDa
Purification Method: Antigen affinity purification

Pax-6 (BD Biosciences 561462): Pax-6 is a member of the paired box (pax) gene family whose protein products are transcription factors involved in development. Pax family members share a highly conserved DNA binding domain that contains six alpha helices (paired domain) and a homeo box domain. Pax-6 has important roles in the development of the eye, nose, central nervous system, and pancreas. Tissue culture supernatant is purified by either protein A/G or affinity purification methods. Both methods yield antibody in solution that is free of most other soluble proteins, lipids, etc. This format provides pure antibody that is suitable for a number of downstream applications including: secondary labeling for flow cytometry or microscopy, ELISA, Western blot, etc.
Reactivity: Human (QC Testing)
Isotype: Mouse BALB/c IgG2a, κ
Clone: O18-1330
Immunogen: Human Pax-6 aa 406-422 Peptide
Molecular Weight: 46-48 kDa

Nkz2.1 (abcam ab76013): Nkx2.1 is a transcription factor with a molecular mass of approximately 38 kDa. It plays a significant role in regulating gene expression. This target is mainly expressed in tissues such as the thyroid lung and the brain.
Host species: Rabbit
Clonality: Monoclonal
Clone number: EP1584Y
Isotype: IgG
Reacts with: Mouse, Rat, Human
Purification technique: Affinity purification Protein A
Observed Molecular Weight: 40 kDa

CTIP2 (Abcam ab18465): CTIP2, also known as BCL11B, is a transcription factor crucial in neuro research for its role in neural development and differentiation. It is particularly important for the development of medium spiny neurons (MSNs) in the striatum, which are essential for motor control and are affected in conditions like Huntington's disease. CTIP2 regulates gene expression involved in neuronal differentiation, axon guidance and synaptic connectivity, making it vital for understanding the cellular architecture and function of the nervous system.
Isotype: IgG2a
Host species: Rat
Clonality: Monoclonal
Clone number: 25B6
Purification technique: Multi-step chromatography
Specificity: Detects 2 bands representing Ctip2 at about 120kD. Ctip2 is highly expressed in brain and in malignant T-cell lines derived

from patients with adult T-cell leukemia/lymphoma
Predicted band size: 96 kDa
Observed band size: ~100 kDa

Brn2 (Thermofisher PA530124): This gene encodes a member of the POU-III class of neural transcription factors. The encoded protein is involved in neuronal differentiation and enhances the activation of corticotropin-releasing hormone regulated genes. Overexpression of this protein is associated with an increase in the proliferation of melanoma cells.
Species Reactivity:Chimpanzee, Human, Mouse, Non-human primate, Rat
Host/Isotype: Rabbit / IgG
Class: Polyclonal
Immunogen: Recombinant protein encompassing a sequence within the C-terminus region of human Brn2.
Purification: Antigen affinity chromatography

Gaba (Thermo Fisher Scientific PA5-32241): This chemical acts as a neurotransmitter in the central nervous system. It reduces neuronal excitation and regulates muscle tone.
Species Reactivity: Chemical, Human, Mouse
Host/Isotype:Rabbit / IgG
Class: Polyclonal
Immunogen: GABA.
Purification: Antigen affinity chromatography

Antibodies used for human brain organoids:
Gephyrin (Synaptic Systems 147 011): Gephyrin is a scaffolding protein associated with inhibitory neurotransmitter receptors
Clone: mAb7a
Subtype: IgG1 (κ light chain)
Immunogen: Nativ Protein corresponding to AA 1 to 768 from rat Gephyrin
Epitop: AA 264 to 276 from rat Gephyrin
Reactivity: human, rat, mouse, pig, goldfish, zebrafish, chicken
Specificity: Specific for the brain specific 93 kDa splice variant phosphorylated at Ser-270. validated PubMed: 9812897

MAP2 (Invitrogen PA1-10005): MAP2 (Microtubule Associated Protein 2) exists in two high molecular weight forms (MAP2a & MAP2b) and a low molecular weight form. The expression of MAP2 is developmentally regulated and its multiple forms arise by alternative splicing of a single gene. MAP2 is involved in microtubule assembly, which is an essential step in neurogenesis. The products of similar genes in rat and mouse are neuron-specific cytoskeletal proteins that are enriched in dendrites, implicating a role in determining and stabilizing dendritic shape during neuron development.
Species Reactivity: Human, Mouse, Rat
Published species: Human, Mouse, Pig, Rat
Host/Isotype: Chicken / IgY
Class: Polyclonal
Immunogen: Mix of recombinant human constructs of projection domain sequences, amino acids 235-1588.
Western blot was performed using Anti-MAP2 Polyclonal Antibody (Product # PA1-10005) and a 160 kDa band corresponding to MAP2 was observed across Mouse Brain and Rat Brain and not in Mouse Heart and Mouse Skeletal Muscle.
Observed Molecular Weight: ~160 kDa

GFAP (Dako Z0334): GFAP (Glial Fibrillary Acidic Protein) is a key marker in neuro research, particularly for its role in identifying astrocyte activity. It is predominantly expressed in astrocytes, the most abundant glial cells in the brain and spinal cord.
Clone: polyclonal
Immunogen: GFAP isolated from cow spinal cord
Species: Rabbit Anit-
Specificity: The antibody has been solid-phase absorbed with human and cow serum proteins. In crossed immunoelectrophoresis using 50 µL antibody per cm2 gel area, no reaction with 2 µL human plasma and 2 µL cow serum is observed. The antibody shows one distinct precipitate (GFAP) with cow brain extract. Staining: Coomassie Brilliant Blue. In indirect ELISA, the antibody shows no reaction with human plasma and cow serum. GFAP shows 90-95% homology between species, and as demonstrated by immunohistochemistry, the antibody reacts strongly with human GFAP.

O4 (R&D MAB1326): Oligodendrocyte Marker O4. Oligodendrocytes are myelinating cells in the central nervous system (CNS) and form the myelin sheath of axons to support rapid nerve conduction. Oligodendrocyte Marker O4 is an antigen on the surface of oligodendrocyte progenitors (1, 2). It has been commonly used as the earliest recognized marker specific for the oligodendroglial lineage Species Reactivity: Human/Mouse/Rat/Chicken
Specificity: Detects human, mouse, rat, and chicken Oligodendrocyte Marker O4.
Source Monoclonal: Mouse IgM Clone # O4
Purification: IgM¬specific Affinity¬purified from hybridoma culture supernatant
Immunogen: Bovine brain corpus callosum white matter

Eukaryotic cell lines

Policy information about cell lines and Sex and Gender in Research

Cell line source(s)	Three mouse embryonic stem cell lines were used: (1) C57BL/6 genetic background (BRUCE-4 ES Cells; Millipore Sigma); (2) E14TG2a (ATCC deposited by T. Doetschman), and (3) KH2 (Jaenisch; https://doi.org/10.1002/gene.20180). Two human iPSC lines used: (1) F12442.4 (Karch; https://doi.org/10.1186/s13195-018-0400-0); (2)NIBSC8 (National Institute for Biological Standards and Control, NIBSC, UK).

Authentication	Mouse ESCs were characterized using standard methods, and validated using qPCR and immunohistochemistry to assess pluripotency and correct cell type patterning. Additional single cell and bulk RNA sequencing was performed to authenticate pluripotency and correct cell type patterning of our organoids. Human iPSC line 1 was analyzed for pluripotency markers and chromosomal abnormalities by G-band karyotyping and were confirmed to possess the appropriate genotype by Sanger sequencing. Human iPSC line 2 was analyzed for genetic stability every 10 passages using the qPCR-based hPSC Genetic Analysis kit (StemCell Technologies™) and authenticated by Short Tandem Repeat profiling.
Mycoplasma contamination	Mycoplasma testing was routinely performed on our ESCs, iPSCs and organoids and all tested negative
Commonly misidentified lines (See ICLAC register)	No commonly misidentified cell lines were used.

Animals and other research organisms

Policy information about studies involving animals; ARRIVE guidelines recommended for reporting animal research, and Sex and Gender in Research

Laboratory animals	mouse C57BL/6JRj from Janvier Labs (P12-14; both sexes)
Wild animals	n/a
Reporting on sex	Neonatal cortical slices were used from both sexes. We do not consider sex as a factor in our analyses, but results apply to all animals studied.
Field-collected samples	No field collected samples were used in the study
Ethics oversight	All experiments involving murine neonatal acute slice recordings were approved by the Basel-Stadt veterinary office according to Swiss federal laws on animal welfare.

Note that full information on the approval of the study protocol must also be provided in the manuscript.

Plants

Seed stocks	n/a
Novel plant genotypes	n/a
Authentication	n/a